The timing of the postglacial marine transgression in the Ría de Ferrol (NW Iberia): A new multiproxy approach from its sedimentary infill

C. Muñoz Sobrino [a,b,*], V. Cartelle [a,c,d], N. Martínez-Carreño [a,d], P. Ramil-Rego [e], S. García Gil [a,d]

[a] *Centro de Investigación Mariña, Universidade de Vigo, Spain*
[b] *Dept. Bioloxía Vexetal Ciencias do Solo, Universidade de Vigo, Spain*
[c] *School of Earth and Environment, University of Leeds, UK*
[d] *Dept. Xeociencias Mariñas, Universidade de Vigo, Spain*
[e] *Gl-1934-TB, Laboratorio de Botánica e Bioxeografía, IBADER, Universidade de Santiago de Compostela, Lugo, Spain*

A B S T R A C T

The Ría de Ferrol is a confined tide-dominated incised valley in the mesotidal passive Atlantic margin of NW Iberia. A new multidisciplinary approach enables a high-resolution reconstruction of the main environmental changes affecting this area during the Lateglacial and the Holocene. We defined the main seismic and sedimentary facies in the infill and selected different key points to be cored. A number of multiproxy analyses were performed on four sections of sediment (sedimentology, X-ray fluorescence, radiocarbon dating and palynological analyses). Physiography exerted a strong control on the evolution of the basin, as a rock-bounded narrow channel in the middle of the basin influenced the flooding of the ria during the postglacial marine transgression. Depositional environments shifted towards the east as the sea level rose and fluvial facies at the base were covered by facies from a tide-dominated estuary, which were predominant during most of the Holocene. Several layers of sediments from stagnant freshwater areas dominated by *Juncus* sp. were recovered at ca. −20.5 to −21, ca. −13.1 to −13.5, −12.5 to −12.8 and −12.1 to −13.5 m NMMA along the central axis of the embayment, and dated to be older than 10190–10290; 10790–10970; 7510–8220 and 7130–7830 cal yr BP. They may respectively represent a local stage of lowering sea-level dated at the end of the Lateglacial (i.e. the Younger Dryas), and different episodes of deceleration/stabilization of sea-level rise occurred during the early Holocene (i.e. the 11.4, 10.5, 9.3, 8.2 kyr Henrich events). Thus, for the first time in this region, we were able to generate a high-resolution spatial–temporal interpretation of environmental changes linked to the relative sea-level variations using subtidal sediments from the same sub-basin (and thus free of substantial/differential post-depositional deformations) that describes in detail the flooding of the ancient coastal plains of this region at the beginning of the Holocene.

1. Introduction

In the actual context of global change and accelerated sea-level rise, a good part of the current coastal salt marshes and other associated ecosystems are in danger of disappearing, threatened by anthropogenic and natural stressors. However, paleo-evidence achieved in estuarine systems worldwide suggests that part of these coastal ecosystems have already survived other accelerated sea level rises in the past (Crosby et al., 2020). Therefore, high-resolution spatial–temporal reconstructions of past changes in estuarine environments may be valuable tools for modelling, predicting and managing the changes to come (Rodríguez et al., 2017; Fagherazzi et al., 2020).

A first step to perform useful reconstructions is to try to unravel global, regional and local forcings and trends. Despite millennial-scale models of relative sea level (RSL) show good agreement in different locations around the world, some differences exist on centennial time scales in the behaviour of the regional sea level and any non-linear sea-level fluctuations (e.g. Peltier, 2001). This variability implies that sea-level oscillations (i.e. the level of the sea surface without reference to the land) are not always equivalent to the level of the sea as observed at the coastline, i.e. the RSL. Dissimilarities may be largely attributed to different local vertical tectonic movements, eustatic variations and the impact of climatic fluctuations on ocean temperature and salinity (e.g. Smith et al., 2011). Besides, the regional palaeogeography and

---

palaeobathymetry also may be influential by determining changes in the tidal range (Shennan and Horton, 2002; Vink et al., 2007).

Estuarine wetlands are complex successions of natural habitats developed between the freshwater coastal ecosystems and the subtidal zone. Therefore, most modern reconstructions of changes in the RSL are based on the identification and description of valuable regional sea-level index points (SLIPs) in coastal areas. They are preferentially thin datable basal peats (frequently ancient estuarine wetlands), intercalated in the sedimentary sequences, but practically unaffected by compaction, and often interpreted as short-term phases of stillstands or slowdowns occurred during long-term phases of sea-level rise (Bungenstock and Schäfer, 2009). Besides, SLIPs enable comparisons with other nearby points susceptible to compaction (e.g. Gehrels, 1999).

The estuarine freshwater peats form at approximately the level of mean high-water spring tides (MHWST) or above it (Shennan and Horton, 2002). Consequently, the age of a freshwater swamp peat is a limiting date in that regional RSL must have been at or below the height of that peat layer (e.g. Shennan and Horton, 2002). Nevertheless, the local occurrence of freshwater peats does not always imply relevant sea-level fluctuations, because other local factors related to each basin's sedimentary dynamics (e.g. the total sediment input or some specific regional palaeogeographic conditions) can also be relevant. When sediment supply exceeds the creation of accommodation space by RSL rise, tidal basins will rapidly accrete sediment to high-water levels. As

tidal inundation becomes less frequent, drainage channels tend to silt up, saltmarshes colonize mudflats and, eventually, peat accumulates (Baeteman et al., 2011).

On the other hand, estuarine wetlands are very unstable, being permanently threatened by eventual sea-level rises and by changes in the input of freshwater and sediment transported from the inland catchments to the coast (e.g. Silva et al., 2007; Perillo et al., 2009; Paterson et al., 2011; Muñoz Sobrino et al., 2014). During periods of rapid subsidence, higher tidal flow velocities and wave energy may erode the outer edge of salt marshes and mudflats; and with rising tidal levels and enough space available, the temperate coastal wetland habitats tend to advance landwards (Pratolongo et al., 2009). Thus, the preservation of useful SLIPs on the emerged shorelines may be irregular, unpredictable and ephemeral (e.g. Gómez-Orellana et al., 2021); and, consequently, the reconstruction of rapid successional changes affecting local or regional coastal wetlands may be sometimes complicated. Identifying short (centennial, decadal) episodes of deceleration (or even minor declines) of RSL may be particularly obscured when occurred inside longer cycles of fast sea-level rise, e.g. the last deglaciation and the early Holocene. Finally, reconstructions performed using different regional SLIPs located on different limnetic contexts may be imprecise because of the difficulty to quantify/correlate other important intervening factors such as compaction, neotectonic and palaeotidal range (e. g. Alonso and Pagés, 2010).
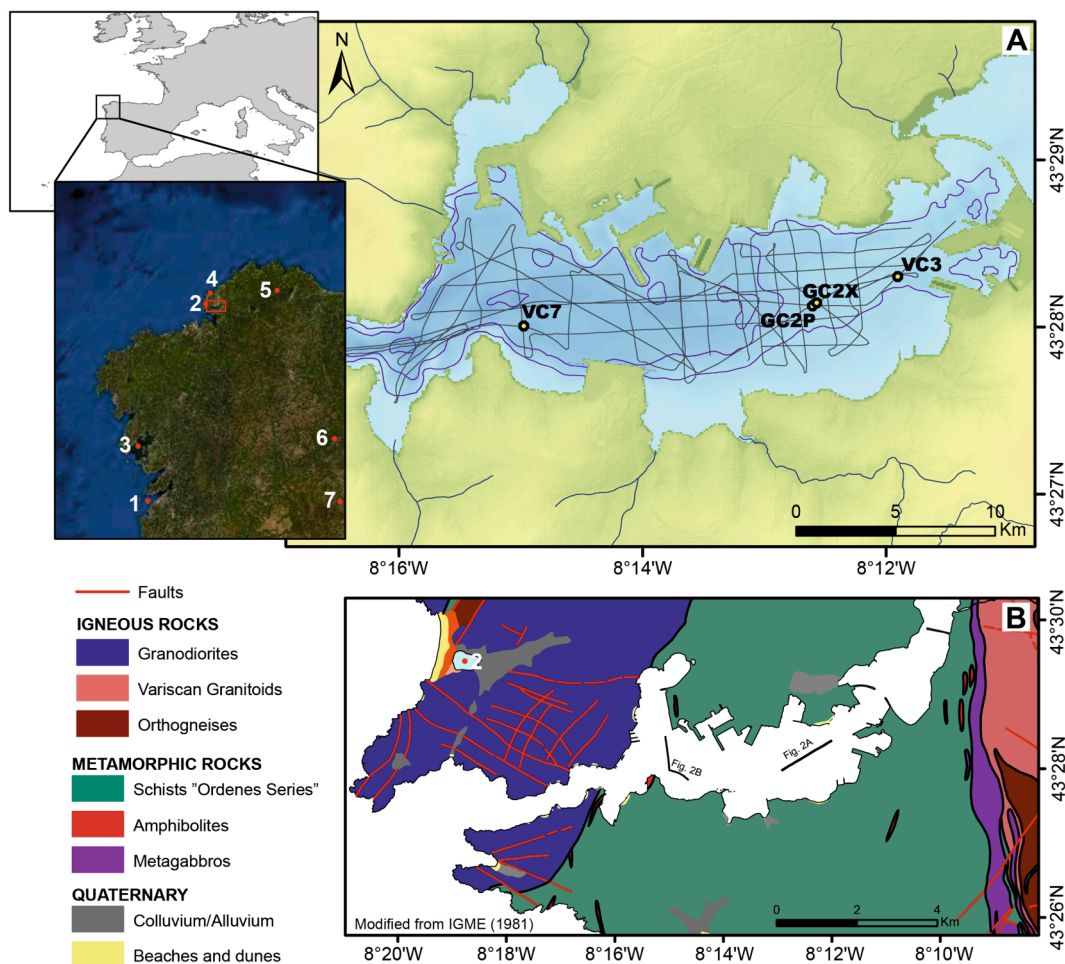
Fig. 1. (A) Location of the study area, showing seismic tracklines and vibro/gravity core positioning: VC7, CGPX, CGP2 and VC3. (B) Map with the emerged geology of the Ría de Ferrol, showing the selected seismic profiles to illustrate architectural elements. Situation of other regional sites discussed in the text: (1) Martínez-Carreño and García-Gil (2017), García-Moreiras et al. (2015, 2019a), Muñoz Sobrino et al. (2007, 2016, 2018); (2) Sáez et al. (2018); (3) García-Moreiras et al. (2019b); (4) Gómez-Orellana et al. (2021); (5) Iriarte-Chiapusso et al. (2016), Muñoz Sobrino et al. (2005, 2007, 2009); (6) Muñoz Sobrino et al. (2001, 2007); Iriarte-Chiapusso et al. (2016); (7) Muñoz Sobrino et al. (2013), Heiri et al. (2014).

Alternatively, some multi-decadal to centennial sea-level fluctuations on different time scales may also be preserved in the subtidal coastal palaeo-records of deltaic regions (e.g. Kearney, 2001; Behre, 2007; García-Gil et al., 2011; Smith et al., 2011; Muñoz Sobrino et al., 2018; García-Moreiras et al., 2019a, 2019b). Particularly, incised valleys (e.g. Boyd et al., 2006) are stratigraphic entities that in the context of coastal systems form in response to a regional decrease in RSL, and develop under two fairly distinct phases: one dominated by fluvial processes during valley incision, and another influenced by fluvial, estuarine, and marine processes during subsequent infilling of the valley. Galician rias are submerged incised valleys located on the NW coast of the Iberian Peninsula (Fig. 1A). Their sedimentary infill has been recently demonstrated to be result of multiple cycles of incision and deposition (Martínez-Carreño and García-Gil, 2017; Muñoz Sobrino et al., 2018; García-Moreiras et al., 2019a; Cartelle et al., 2019). Besides, incised valleys may record high-frequency climatic fluctuations and extreme events (e.g. Troiani et al., 2011; Sorrel et al., 2012; Baltzer et al., 2014; Poirier et al., 2017) that became especially important when the rate of relative sea-level rise decreased after 6000–5000 yr BP as local factors played a more significant role in coastal evolution (e.g. Goy et al., 1996; Bao et al., 1999; Muñoz Sobrino et al., 2012, 2014, 2016; García-Moreiras et al., 2018).

Sediment stacked during those cycles may include evidence of different ecosystems (subtidal, mudflats, low marsh, high marsh, freshwater peat, etc), but their spatial distributions and rapid temporal changes can hardly be reconstructed using geophysical evidence. Analyses of the sediment content in pollen, dinoflagellate cysts and other non-pollen palynomorphs (NPP) assist in obtaining a better characterization of sedimentary environments. Nevertheless, some types of coastal habitats (e.g. rush or sedge ecosystems) can be challenging to detect by microremain analyses because they usually lack a clear distinctive signal (e.g. Marsh and Cohen, 2008; García-Moreiras et al., 2015).

X-ray fluorescence (XRF) analysers provide the elemental composition of a wide range of environmental materials (e.g. Boyle, 2000), and XRF data enable to address sedimentological facies and textural characteristics of sediments. In mixed sediments, these methods allows discriminating between autochthonous and allochthonous inputs. Therefore, XRF has been used with different goals, frequently combined with pollen data and other proxies, in both continental (e.g. Turner et al., 2015), fluvial (e.g. Dupont and Kuhlmann, 2017), marine (e.g. Zhao et al., 2019) and coastal (e.g. Emmanouilidis et al., 2020) sedimentary systems. But as far as we know, XRF-data and pollen evidence have never been combined before to detect the spatial–temporal changes of several salt marsh communities (rushes, sedges) that usually only leave feeble signals in the sedimentary record.

Here we present and discuss the results of a multiproxy approach that combines seismic profiles and sedimentary sequences obtained from a subtidal area of an inner embayment in the Ria de Ferrol, NW Iberia (Fig. 1). The new methodology proposed (analyses of microremains combined with XRF data) allows better differentiation between subtidal environments, mudflats, salt marshes and estuarine freshwater swamps. Thus, the new data obtained serve to advance in the development of the seismic interpretation of sedimentary fills (previously performed by Cartelle et al., 2019) by increasing the spatial–temporal resolution and other environmental details relative to the uppermost seismic facies in the basin. Four organic-rich sections (VC7, GC2X, GC2P, VC3; Fig. 1) from the subtidal zone are studied, revealing several rapid regional oscillations in the RSL during the Lateglacial-Holocene transition. This evidence is compared with other multiproxy studies in NW Iberia (e.g. Muñoz obrino et al., 2013, 2018; Sáez et al., 2018; García-Moreiras et al. 2019a, 2019b; Gómez-Orellana et al., 2021) that can support a more comprehensive interpretation of the main changes affecting the regional climate, hydrology and vegetation, especially from the end of the Last Glacial Maximum (LGM) to the Holocene Climatic Optimum. Besides, environmental changes reconstructed at the seashore may also contribute to explain the dynamics observed in the nearby coastal mountains (e.g. Muñoz Sobrino et al., 2005, 2009; Iriarte-Chiapusso et al., 2016).

2. Study area

2.1. Ría de Ferrol: Geography and geological context

Galician rias are located on the eastern passive Atlantic margin of Galicia (NW Iberia) and comprise both the *Rías Altas* to the north of Cape Finisterre and the *Rías Baixas* to the south (Fig. 1). The Ría de Ferrol (RdF, total area of 21 km^2) forms part of the Ártabro Gulf together with the rias of A Coruña and Ares-Betanzos (Fig. 1). Currently, the RdF is protected from swell and storm events by its morphology and ENE–WSW orientation, although three main physiographic areas can be distinguished inside it (Fig. 1): a) a NE-SW-oriented outer sector that connects the ria to the mouth of the Ártabro Gulf; b) a 2.7 km long, 0.5 km wide channel (Ferrol Strait) connecting the outer and inner sectors; and c) an inner sector that begins with an E-W orientation but changes to NE-SW in several small bays appearing in its innermost part.

Water depths in RdF vary from <5 m in its innermost area to 35 m near its mouth, with an average depth of 20 m in the strait (Fig. 1). The main freshwater inputs to RdF are the Xubia and Belelle rivers, both discharging a total mean of 6 m^{3}s^{-1} (deCastro et al., 2004) in the innermost sector. Besides, other minor freshwater streams also flow into the middle parts. Biogenic sands and gravels mainly dominate the seabed sediments of the outer and strait sectors, while the highly organic mud fraction reaches 20% in the inner sector (Cobelo-García and Prego, 2004).

The geology of the Galician coast is characterized by granites and Palaeozoic sedimentary rocks metamorphosed during the Variscan orogeny. These rocks form alternating bands cut by NE-SW, N-S and NW-SE faults (IGME, 1981). The outer sector and the strait of the RdF (Fig. 1B) are placed within an NNE–SSW band of granitic rocks (mainly granodiorites and orthogneisses), and the inner sector is located within the uppermost units of the Ordenes Complex (gneisses, amphibolites and gabbros). Sandy and silty sediments from rivers, beaches and coastal dunes are the main Quaternary deposits (IGME, 1981).

2.2. Climate, oceanography and tides

The main synoptic weather types in NW Iberia results from a combination of the North Hemisphere Annular Mode (NAM) and different large-scale atmospheric modes, namely the North Atlantic Oscillation (NAO), the Eastern Atlantic (EA), the Eastern Atlantic/Western Russia (EA/WR), and the Scandinavian Pattern (SCA). Most rainfall throughout the year can be explained by cyclonic, western and south-western weather types. A positive NAO index greatly reduces the occurrence of cyclonic weather in winter, but the EA mode has a positive annual correlation with W and SW weather types that produce increasing rainfall in spring, summer and autumn (e.g. Lorenzo et al., 2008).

All the Iberian Atlantic shore (Fig. 1A) is situated at the northern margin of the NW African coastal upwelling system and is under the influence of the Eastern North Atlantic Central Water (ENACW). Therefore, the influence of upwelling is intense on most of the western Iberian coast, where observed sea-surface temperatures (SST) trends are related to changes in upwelling dynamics or in radiative or atmospheric heat fluxes (Alvarez et al., 2011; Alves and Miranda 2013). The Portugal Current System (PCS) flowing towards the Equator in summer and towards the Arctic in winter dominates the surface offshore western Iberian waters (Sprangers et al., 2004; Otero et al., 2008). Two ENACW branches flow under the PCS, namely the subtropical (ENACWst) and subpolar (ENACWsp) waters. The Mediterranean Water (MW), highly saline and relatively warm, flows northwards between ca. 550–1600 m depth and along the Iberian coast. The deepest waters offshore are nutrient-rich and oxygen-poor bottom masses, like the North Atlantic

Deep Water (NADW) and the lower-saline Labrador Sea Water (LSW) (e. g. Muñoz Sobrino et al., 2014; García-Moreiras et al., 2018).

Tides in the RdF is mesotidal and semidiurnal, with amplitudes ranging from 1.5 m (neap tides) to 4.0 m (spring tides). Hydrodynamics are strongly influenced by the particular physiography of the ria, making it different to the rest of the Galician rias. While the *Rías Baixas* (Fig. 1A) are generally stratified with a circulation pattern in two layers (Barton et al., 2015), only the inner sector in the RdF is partially stratified. In the RdF, water circulation is mainly controlled by tides, as the tidal prism represents up to 30% of the ria volume (deCastro et al., 2003), and the strait and outer sectors are well mixed due to high tidal velocities (deCastro et al., 2004). Another critical difference is that most of the other Galician rias are frequently affected by upwelling events (Fraga, 1981; Gómez-Gesteira et al., 2001; Prego et al., 2001; Barton et al., 2015), but those in the Ártabro Gulf remain isolated from upwelled waters (Prego and Varela, 1998).

2.3. Climate and RSL between the LGM and the Early-Holocene

The climatic pattern over the North Atlantic described above become probably disrupted during the LGM (e.g. Justino and Peltier, 2005) and substantially modified during the Lateglacial and the Early Holocene (e. g. Muñoz Sobrino et al., 2013; Matero et al., 2017; Rea et al., 2020). These changes also affected the coastal upwelling systems (e.g. Abrantes, 1991; García-Moreiras et al., 2019a, 2019b), and evidence (van der Knaap and van Leeuwen, 1997; Roucoux et al., 2001; Muñoz Sobrino et al., 2005, 2009, 2013; Iriarte-Chiapusso et al., 2016) suggests that marine changing conditions also contribute to govern the postglacial vegetation dynamics inland.

Evidence of rapid climate variability between ca. 14.7–8.0 kyr BP over the North Atlantic (e.g. Moreno et al., 2014; Heiri et al., 2014; Wanner et al., 2015) and NW Iberia (e.g. Muñoz Sobrino et al., 2013; Iriarte-Chiapusso et al., 2016; García-Moreiras et al., 2019b), includes two notable periods of cool temperatures before (Oldest Dryas, GS2a: >14640 cal yr BP) and after (Younger Dryas, GS-1: 12730–11650 cal yr BP) the Lateglacial Interstadial (GI1: 14640–12730 cal yr BP); and also several short regional colder events during the GI1 and the Early-Holocene: Older Dryas (GI-1d: 14250–14050 cal yr BP), La Roya-I (GI-1c2: 13600–13400 cal yr BP), La Roya-II (GI-1b: 13300–12900 cal yr BP), 11.4 event (11400–11100 cal yr BP), 10.5 event (10290–10240 cal yr BP), 9.3 event (9260–9230 cal yr BP) and 8.2 event (8360–8050 cal yr BP). Most of them were probably connected to the advection of southward and eastward drifting surface water from the Nordic and Labrador Seas, which gave rise to century-scale cold relapses (Bond events) in the North Atlantic and European regions (Bond et al., 1997).

These postglacial climate oscillations modified the volume of continental ice and changed the sea level. The data available in NW Iberia (e. g. Dias et al., 2000; Leorri et al., 2013; Martínez-Carreño and García-Gil, 2017) point to a phase of rapid increase of the sea level, from 130 m bmsl (below modern sea-level) at the LGM to about 26 m bmsl at the beginning of the Holocene (11.2–9.4 cal kyr BP). Between 9.4 and 6.8 cal kyr BP the sea level rose up to 5 m bmsl, and then (6.8–4.2 cal. ka BP) stabilized. The last stage of relative sea-level rise occurred between 4.2 and 0 cal ka BP.

3. Methodology

3.1. Seismic surveys and coring

Seismic data and cores presented were obtained during two surveys (ECOMER14 and ECOMER15) developed from 2014 to 2015 on-board the *R/V Mytilus* (Consejo Superior de Investigación Científica) and the Amarradores Mil (Amarradores del Puerto y Ría de Ferrol, S.L.), respectively. Up to 105.8 km of high-resolution seismic records were acquired covering the outer and inner sectors (Fig. 1A). Besides, several gravity cores and vibro-cores were recovered from selected sites

(Fig. 1A; see details in Cartelle et al., 2019). Sedimentary and other multiproxy data discussed here only corresponds to four selected sections of sediment located in the innermost part of the RdF (Fig. 1A; Table 1). Both the gravity and vibro-corer used consisted of a 4-m long, 9-cm diameter steel core barrel. The depth of the cores and samples is referred to the NMMA (the mean sea level in Alicante), which is the Spanish orthometric datum defined on the Mediterranean coast. The reference level of NMMA is 0.29 m below local modern mean sea level in the RdF.

The seismic data were acquired using a 'modified Boomer', with a single Boomer source (AAE CSP 300 and AA200) and two receivers (the ceramics of a sub-bottom profiler and a single channel streamer). A differential global positioning system (dGPS) using an AgGPS 132 receiver were used for positioning (error < 1 m). Seismic profiles were integrated into IHS Kingdom Suite software for interpretation.

3.2. Grain size and geochemical analyses

Sediment cores were split lengthwise in the laboratory, described and sampled for analysis. Detailed information about these analyses is available in Cartelle et al. (2019). All of the analyses were performed in the CACTI laboratory (Universidade de Vigo). One half was subjected to non-destructive analysis using an ITRAX core scanner providing X-ray fluorescence (XRF) elemental data. Particle size distribution was characterized by laser diffraction and the results were classified following the nomenclature of Wentworth (1922).

3.3. Chronologies

When possible, well-preserved articulated valves without signatures of reworking were selected for radiocarbon dating, but on occasion, small remains of wood and very organic bulk sediment from some location free of biogas (see Muñoz Sobrino et al., 2014) were also used (Table 2). The analyses were performed at Beta Analytic Laboratory in Miami, USA. All radiocarbon dates are given in calibrated years before present (cal yr BP) after calibration using CALIB 8.2 (Stuiver et al., 2020). For bivalve and gastropod shells, the Marine20 radiocarbon calibration curve was used (Heaton et al., 2020), with a minor local reservoir correction (Soares and Dias, 2007; see Table 2) because the area is not affected by older upwelled waters or ^{14}C depleted surface runoff, as the drainage basin lacks carbonate rocks. For wood material, the IntCal20 database was used (Reimer et al., 2020). Finally, the mixed Marine & NH Atmosphere (50:50) of calibration of Stuiver et al. (2020) was used to date on bulk sediment (see Muñoz Sobrino et al., 2014). Pollen-inferred ages for the onset of the Lateglacial Interstadial, the onset and end of the Younger Dryas (YD), and the onset of other well-recognised regionally dated cold-events (namely 11.4 ka, 9.3 ka, and 8.2 ka) were also used when possible (Table 3 Rasmussen et al., 2014), to develop comparable spline. Finally, for the most recent periods, other chronological inferences could be made from the results of the XRF analyses and the interpretation of selected pollen curves (Fig. 4 and Table 3; see discussion).

3.4. Integration of seismic and sedimentary facies

Seismic data follows Cartelle et al. (2019) and were interpreted according to the basic principles of seismic stratigraphy (e.g. Mitchum et al., 1977). The sediment cores were tied to seismic records, allowing facies and radiocarbon dates to be correlated with seismic units (Figs. 2 and 3). Core compaction was corrected by calculating the ratio between total corer penetration and core recovery (Table 1). A sound velocity of 1500 ms^{-1} for saltwater and 1600 ms^{-1} for unconsolidated sediments was assumed for time to depth conversion (Hamilton, 1980; Hamilton and Bachman, 1982).

Table 1

Cores studied in the Ría de Ferrol, indicating position, length, water depth, the seismic units recovered and the sections in which multiproxy analyses have been made. Water depth is expressed as m NMMA corresponds to the differences respect to the mean sea level in Alicante, i.e., the Spanish orthometric datum.

Core	Survey	Position (UTM)		Laboratory length (m)	Water depth (m NMMA)	Seismic units recovered	Grain size and geochemical analysis	ITRAX	Pollen analyses sections (cm)
		X	Y						
GC2X	ECOMER-2014	563962,5	4813236,3	2.87	−10.7	U7/U6	YES	YES	200–285
GC2P	ECOMER-2014	563929,017	4813222,13	2.44	−10.5	U7/U6	YES	YES	0–236
VC3	ECOMER-2015	564861,1	4813525,3	3.35	−10.3	U7/U6	YES	YES	160–325
VC7	ECOMER-2015	560721,4	4812982,5	2.26	−18.8	U7/U6	YES	YES	60–220

Table 2

Details of all the radiocarbon dates obtained for the cored studied. All radiocarbon dates are given in calibrated years before present (cal yr BP) after calibration using CALIB 8.2 (Stuiver et al., 2020). For bivalve and gastropod shells, the Marine20 radiocarbon calibration curve was used (Heaton et al., 2020), with a minor a local reservoir correction (Weighted Mean ΔR = 12; Uncertainty = 163) calculated from the 10 closest data available in Stuiver et al. (2020). For wood material, the IntCal20 database was used (Reimer et al., 2020), and the mixed Marine & NH Atmosphere (50:50) of calibration of Stuiver et al. (2020) was used to date on bulk sediment (see Muñoz Sobrino et al., 2014).

Core	Depth in core (cm)	Lab reference	Material dated	Conventional Radiocarbon Age	d13C	d18O	Median proability	2 sigma calibration (Calib)	
VC7	41–42	Beta-438689	Bivalve	1140 ± 30 BP	1,7	1,2	552	239–901	MARINE20
VC7	90–92	Beta-438691	Bivalve	8230 ± 30 BP	−0,5	0,3	8560	8161–9001	MARINE20
VC7	165–166	Beta-505682	Marine Organic Sediment	9090 +/- 30 BP	−26.8		10,237	10193–10290	INTCAL20
GC2X	119–121	Beta-408228	Bivalve	1580 ± 30 BP	1,4	–	961	629–1300	MARINE20
GC2X	184	Beta-421899	Gastropod	6510 ± 30 BP	0,5	–	6771	6377–7165	MARINE20
GC2X	218–220	Beta-408233	Bivalve	7630 ± 30 BP	0,2	–	7899	7562–8274	MARINE20
GC2X	238	Beta-408234	Charred wood	9630 ± 30 BP	−25,2		10,950	10790–10966	INTCAL20
GC2P	129–130	Beta-438692	Bivalve	6360 ± 30 BP	−0,5	0,3	6603	6220–7002	MARINE20
GC2P	136–138	Beta-438690	Bivalve	1480 ± 30 BP	0,6	0,2	864	544–1214	MARINE20
GC2P	167–168	Beta-438694	Bivalve	7320 ± 30 BP	1	0,9	7600	7265–7937	MARINE20
GC2P	185–186	Beta-438695	Bivalve	7590 ± 30 BP	1,4	1,1	7858	7507–8217	MARINE20
VC3	54	Beta-421912	Bivalve	6640 ± 30 BP	1,4	1,6	6916	6516–7293	MARINE20
VC3	105	Beta-421904	Bivalve	6900 ± 30 BP	1,3	1	7189	6808–7539	MARINE20
VC3	135	Beta-421901	Bivalve	7180 ± 30 BP	1	0,9	7466	7130–7826	MARINE20

3.5. Pollen, dinoflagellate cysts and NPP

Palynological analyses were performed on selected sections of sediment (Table 1) obtained from two gravity cores (GC2P: 0–240 cm; GC2X: 200–285 cm) and two vibro-cores (VC3: 160–325 cm; VC7: 60–220 cm). Pollen samples of 1 or 3 cm³ of fresh sediment were prepared using HCl + HF treatment (Moore et al., 1991). Coarse (>250 mm) and fine (<10 mm) fraction sediments were eliminated by sieving. Most of the core sections were subsampled at regular 10-cm intervals, but higher resolution was obtained in key parts of the sequences (sampled at 2-, 3-, 4-, 5- or 6-cm intervals). All samples were spiked with *Lycopodium* spores for absolute palynomorph estimation. The slides were mounted in glycerol and analysed using a Nikon B50 microscope at 400 and 600x magnifications.

A total of 87 samples were analysed, 42 corresponding to the entire GC2P core, with other 21, 14 and 9, respectively, from the different complementary sections studied in cores VC7, GC2X and VC3. A mean of 256 grains of pollen was counted per each GC2P sample (minimum 19, maximum 366), but four of them show low pollen concentrations and therefore result in poor (<90 grain) or very poor (<20 grains) pollen counts. The total pollen sum for the VC7 samples studied ranges between 53 and 401 (204 on average) and between 108 and 567 (308 on average) for GC2X samples. Finally, most of VC3 samples had low pollen concentration and pollen diversity. Dinoflagellate cysts content was low in most samples but notably increases in the uppermost 130 cm of the core GC2P. The percentages of the different types of dinoflagellate cysts (identified groups follow Zonneveld et al., 2013) were calculated in relation to the total dinoflagellate cysts count. Total pollen and dinoflagellate cysts sums are shown (Figs. 5, 6, 7 and 8) to assess percentage

reliability.

Non-pollen palynomorph (NPP) percentages, including mainly microforaminiferal linings (Stancliffe, 2002) and fungal and fresh/brackish-water algae remains (van Geel et al., 1989; van Geel, 2003), were based on total pollen plus NPP. Finally, the ratio of dinoflagellate cyst concentrations to pollen, fern spore and dinoflagellate cyst concentrations (D/P ratio, ranging between 0 and 1; modified as the inversed ratio used by McCarthy and Mudie, 1998) was calculated for each sample to show the temporal variation. TILIA 2.6.1 software (Grimm 1990–2019) was used to process the data and prepare the diagrams. All the pollen records were independently zoned using a constrained incremental sum of squares (CONISS) cluster analysis with Euclidian distance (Figs. 5 to 8). Due to the scarce cyst content of most of the sediment sections studied, their dinoflagellate records were not independently zoned, but their main changes are discussed following their local pollen assemblage zonation (LPAZ).

4. Results

4.1. High-resolution seismic reconstruction of the RdF inner sub-basin

The complete seismic architecture and the facies of the seismic units identified in the RdF have been previously described in detail by Cartelle et al. (2019). The three uppermost seismic units (U5, U6, U7) encompass the most recent sedimentary package in the inner RdF sub-basin, which are studied in more detail here (Fig. 2AB). Unit U5 is very thin (usually < 3 ms two-way travel-time [TWT]) and rests directly above the rocky basement, usually deposited in basement lows, and increases in thickness landward (Cartelle et al., 2019). U5 mainly corresponds to large- to

Table 3

Chronological benchmarks used to build the age-depth models showed in Fig. 4, including radiocarbon dates (see details in Table 2), pollen inferences (Muñoz Sobrino et al., 2007, 2012, 2014, 2016; Iriarte-Chiapusso et al., 2016; García-Moreiras et al., 2019b) and X-ray fluorescence evidence (Moreno et al., 2015). All dates are given in calibrated years before present (cal yr BP). Error range assumed for radiocarbon dates corresponds to two the sigma calibration (Calib). See discussion for details. (*) Rio das Furnas 2 (RF2) corresponds to site 5 in Fig. 1. (**) Both depths have been exchanged (see Table 2) to avoid inversions in the age-depth curves and to estimate the time interval to which the hiatus could correspond. This type of inversions may be expected in the levels of erosion related to the seismic disconformities (see the text).

Core	N^{er} (Fig. 4)	Depth (cm)	Type	Age	Error range	Calibration curve	Events	References
VC7	1	0.5	Surface	−60	−56/−64			
VC7	2	25	Br	270	235/305		Mounder Minimum	Moreno et al., 2015
VC7	3	41.5	^{14}C	552	239/901	MARINE20		
VC/	4	61	^{14}C/Pollen stratigraphy	8257	8072/8356	INTCAL20	8.2 event dated in RF2 (*)	Iriarte-Chiapusso et al., 2016.
VC7	5	90.5	^{14}C	8560	8161/9001	MARINE20		
VC7	6	165.5	^{14}C	10,237	10,193/10,290	INTCAL20		
VC7	7	172	Pollen stratigraphy	10,500	10,237/10,290	INTCAL20	10.5 event	García-Moreiras et al., 2019b
VC7	8	192	Pollen stratigraphy	11,400	10,483/10,735	INTCAL20	11.4 event	Iriarte-Chiapusso et al., 2016.
VC7	9	215	Pollen stratigraphy	11,650	11,487/11,733	INTCAL20	Holocene onset	Iriarte-Chiapusso et al., 2016.
GC2X	10	0.5	Surface	−60	−56/−64			
GC2X	11	120	^{14}C	961	629/1300	MARINE20		
GC2X	12	184	^{14}C	6771	6377/7165	MARINE20		
GC2X	13	219	^{14}C	7899	7562/8274	MARINE20		
GC2X	14	235	^{14}C/Pollen stratigraphy	8257	8072/8356	INTCAL20	8.2 event dated in RF2 (*)	Iriarte-Chiapusso et al., 2016.
GC2X	15	236	Pollen stratigraphy	10,500	10,237/10,290	INTCAL20	10.5 event	García-Moreiras et al., 2019b
GC2X	16	238	^{14}C	10,950	10,790/10,966	INTCAL20		
GC2X	17	276	Pollen stratigraphy	11,400	10,483/10,735	INTCAL20	11.4 event	Iriarte-Chiapusso et al., 2016
GC2P	18	0.5	Surface	−60	−56/−64			
GC2P	19	31	Pollen stratigraphy	−10	−20/10		Repulations with *Eucalyptus*	Muñoz Sobrino et al., 2007, 2012, 2014, 2016
GC2P	20	71	Pollen stratigraphy	230	220/240		Repulations with *Pinus*	Muñoz Sobrino et al., 2007, 2012, 2014, 2016
GC2P	21	73	Br	270	235/305		Mounder Minimum	Moreno et al., 2015
GC2P	22	137(**)	^{14}C	864	544/1214	MARINE20		
GC2P	23	129.5 (**)	^{14}C	6603	6220/7002	MARINE20		
GC2P	24	167.5	^{14}C	7600	7265/7937	MARINE20		
GC2P	25	185.5	^{14}C	7858	7507/8217	MARINE20		
GC2P	26	221	^{14}C/Pollen stratigraphy	8257	8072/8356	INTCAL20	8.2 event dated in RF2 (*)	Iriarte-Chiapusso et al., 2016.
VC3	27	54	^{14}C	6916	6516/7293	MARINE20		
VC3	28	105	^{14}C	7189	6808/7539	MARINE20		
VC3	29	135	^{14}C	7466	7130/7826	MARINE20		
VC3	30	202	^{14}C/Pollen stratigraphy	8257	8072/8356	INTCAL20	8.2 event dated in RF2 (*)	Iriarte-Chiapusso et al., 2016.
VC3	31	321	Pollen stratigraphy	10,500	10,237/10,290	INTCAL20	10.5 event	García-Moreiras et al., 2019b

medium-scale low-sinuosity fluvial channels generally characterized by chaotic seismic facies but sometimes displaying a complex internal structure representing different types of bars (transverse, medial and longitudinal bars) within the channels (Fig. 2).

Unit U6 rests above unconformity D5 (Fig. 2), being generally thicker than U5 but disappearing in the axis of the east-inner sector, where it is deeply eroded by disconformity D6. Deposits of this unit mainly correspond to large-scale estuarine channel fills to the west and tidal mudflats in the margins dissected by small-scale tidal channels. Some thin sheet-like floodplain deposits are also preserved at the base of the unit, mainly to the southeast margin of the inner sector (Fig. 2). The lowermost part of seismic unit U6 was dated to be ca. 10790–11170 cal yr BP, and its top at ca. 5755–5940 cal yr BP (Cartelle et al., 2019).

Unit U7 is the youngest and most extensive, distinguished in the entire sector and affected by acoustic blanking areas (Cartelle et al., 2019). As part of this unit, tidal bars are dominant to the west and close to the strait (Fig. 1), while medium-scale estuarine channel fills appear in the axis covered by a sheet of muddy marine sediments (Fig. 2).

Towards the innermost part, in the east, a small subaqueous fan deposit (bayhead delta) is also preserved. All dates available for U7 are younger than 3670–3860 cal yr BP, but most of the contacts (disconformity D6) between U6 and U7 are abrupt, including discontinuities that extent since before 6000 cal yr BP until the historical period (Cartelle et al., 2019).

4.2. Sedimentology of the core sections selected

Sediment core (Table 1) retrieval was successful in the inner sector at selected sites (Fig. 1A) along the seismic profiles, providing insight into the sedimentary facies of the seismic units and allowing establishing the chronostratigraphic framework. Cores recovered the two youngest seismic units, U6 and U7. Core logs are presented in Fig. 3.

Core VC7 (Fig. 3) is 2.26 m in length and was recovered at a water depth of −18.8 m NMMA in the west of the inner sector (Table 1, Fig. 1A). The basal facies correspond to seismic unit U6 and are composed of two fining-upwards facies successions. The lower package
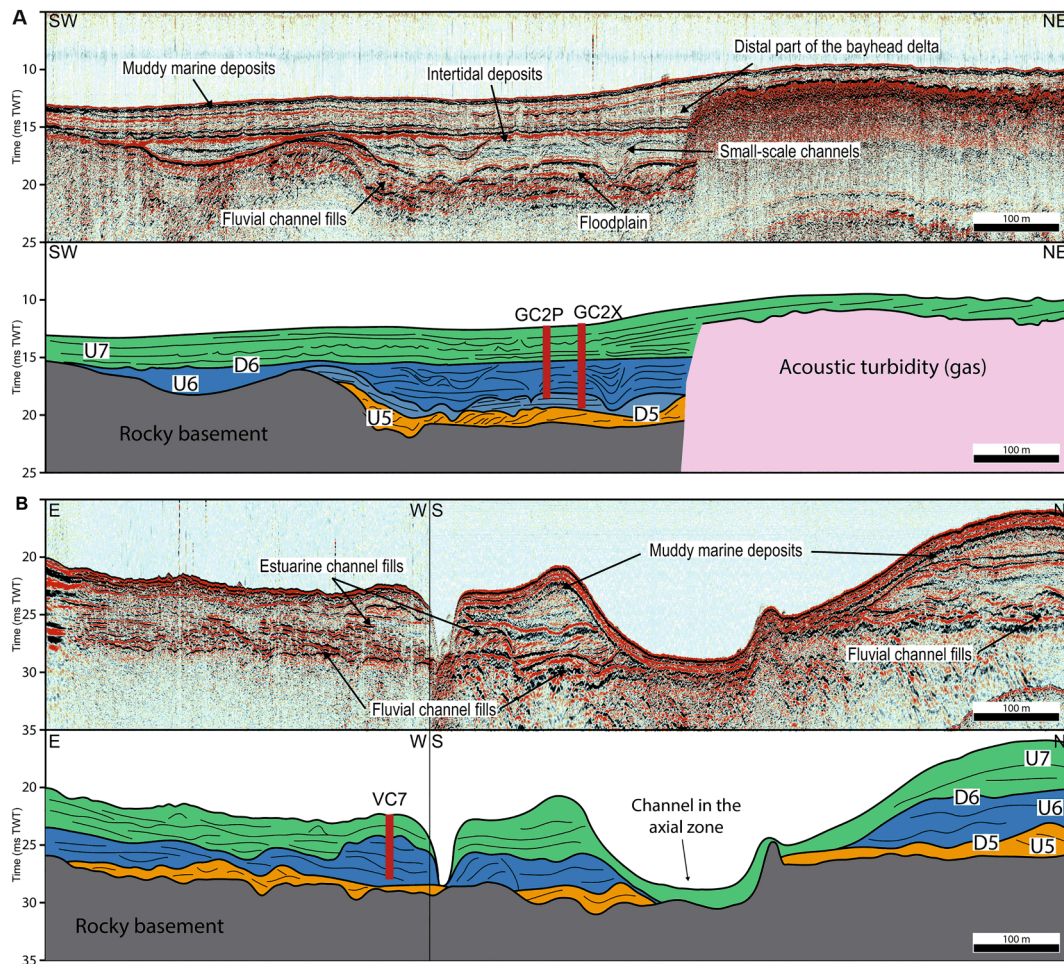
Fig. 2. Seismic records and interpretation sketches in the innermost bay of Ría de Ferrol, showing the identified seismic units (U5 to U7) and their bounding surfaces (D5-transgressive surface, D6-tidal ravinement surface). The preserved architectural elements are also indicated. (A) Seismic profile showing the location of cores GC2X and GC2P. (B) Seismic profile showing the location of core VC7. Seismic notation from Cartelle and García-Gil (2019). TWT: two-way traveltime.

(226–92 cm) corresponds to siliciclastic sediment, grading from rounded gravels (centile 5 cm) at the base (up to 85% gravel) to laminated sandy silt at the top (>50% silt and <30% sand), rich in organic matter with abundant vegetal remains and small bioclastic fragments in the upper 23 cm. The upper package (92–65 cm) begins with a basal lag of bioclastic gravels (3 cm thick) transitioning to laminated silty sand (>75% of sand) with abundant shell fragments. The upper section of the core corresponds to seismic unit U7. The lower package consists of bioclastic gravels (65–43 cm, with abundant oyster shells) with a muddy sand matrix, showing low-angle lamination and a sharp basal erosive contact that coincides with disconformity D6. The upper package (43–0 cm) is bioturbated sandy sediment with increasing silt and clay percentages towards its top.

Core GC2X (Fig. 3) is 2.87 m long and was recovered at a water depth of −10.7 m NMMA in the southern margin of the east of the inner sector (Table 1, Fig. 1A). It reaches the lowermost part of U6, which consists of laminated muddy facies (287–237 cm), mainly composed of clay and silt (>75% mud), rich in vegetal remains and with no carbonate. This facies is light grey to slightly green and became quickly oxidized, turning to ochre once exposed to air. The above package (237–155 cm) is characterized by interbedded deposits of laminated sandy silt (≈70% silt, ≈10-30% sand) and bioclastic gravels (shell fragments). The upper section of the core recovers seismic unit U7, with a sharp and erosive basal contact that coincides with surface D6 from seismic data. The facies succession shows a fining-upwards trend with a package (155–129 cm) of bioclastic gravels (up to 3 cm and high

abundance of oysters) matrix-supported by sand and silt, overlain by highly bioturbated silty sediment (65–75% silt) with increasing percentages of clay towards the top.

Core GC2P (Fig. 3) is 2.41 m long and was recovered at a depth of −10.5 m NMMA at the southern margin of the east inner sector (Table 1; Fig. 1A). Cores GC2P and GC2X are recovered at less than 36 m from each other, and the facies sucession is similar but involving slightly different depth ranges. The lower section of the core recovered seismic unit U6 where two facies associations are distinguished, a lower package (241–200 cm) of laminated grey mud rich in vegetal remains and lacking carbonate, passing upwards (200–146 cm) to interbedded deposits of laminated sandy silt and bioclastic gravels (shell fragments). The upper section of the core recovered seismic unit U7 with a basal erosive contact corresponding to surface D6 from seismic records. The facies succession shows a fining-upwards trend with a package (146–132 cm) of bioclastic gravels matrix supported by sand and silt, overlain (132–0 cm) by slightly bioturbated silty sediment with increasing percentages of clay towards the top.

Core VC3 (Fig. 3) was retrieved at a water depth of −10.3 m NMMA from the eastern part of the inner sector and had a length of 3.35 m (Table 1, Fig. 1C). The lower section of the core recovers seismic unit U6, where three facies associations are distinguished. The lower package (335–145 cm) corresponds to laminated grey to greenish mud lacking carbonate that quickly oxidizes once exposed to the air. This package displays embedded black-coloured organic clasts and rounded siliciclastic gravels (up to 1.5 cm of diameter). Above a fining upwards facies
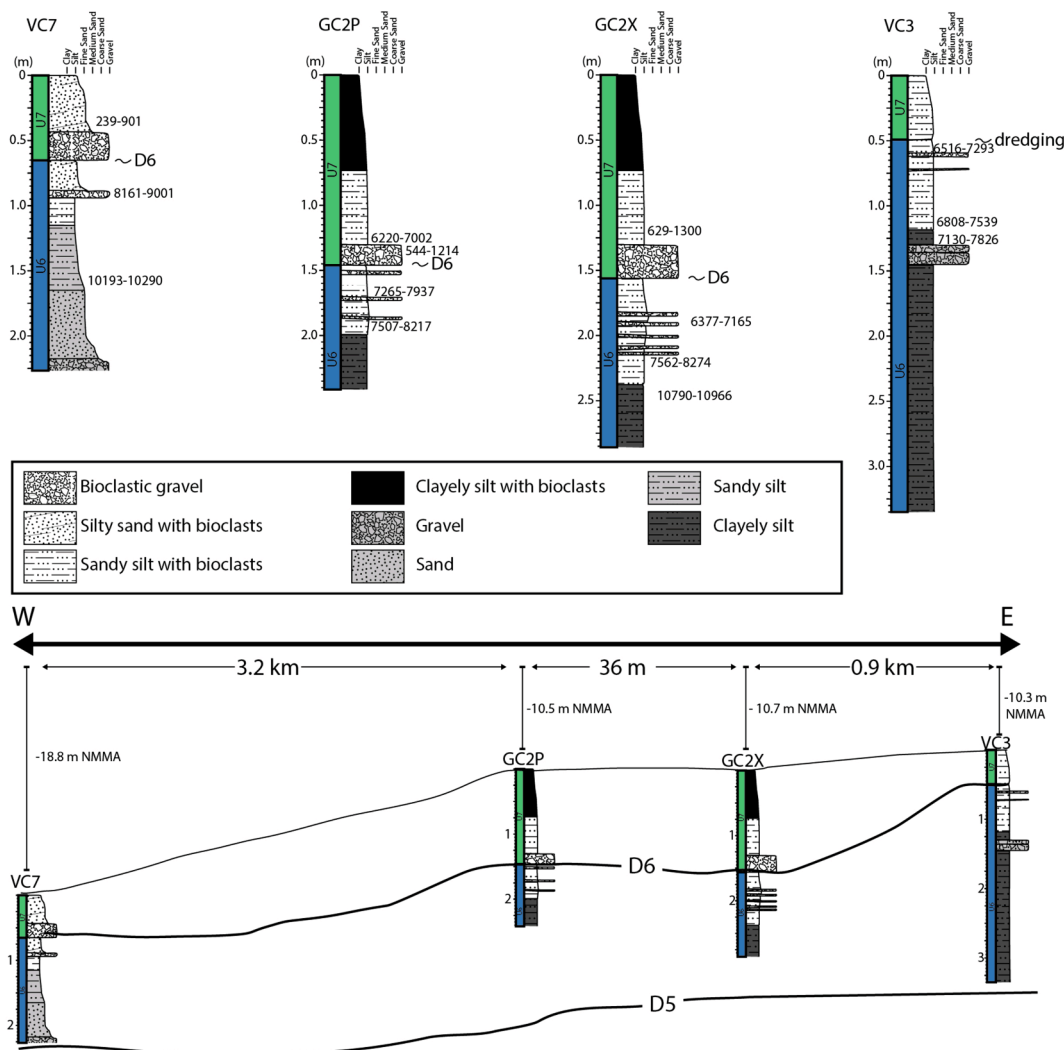
Fig. 3. Sedimentary facies, radiocarbon dates and spatial correlations between the four cores discussed: VC7, CGPX, CG2P and VC3. Interpretations of depositional environments are also shown following the architectural elements described by Cartelle and García-Gil (2019).

succession (145–122 cm) is distinguished with basal rounded silici-clastic gravels (centile 5 cm) in a matrix of grey silt and sand; passing to grain-supported siliciclastic gravels (centile 1 cm), sub-rounded and medium selected with cm-scale bioclastic fragment in a matrix of sand; and finally grey mud with high water content. The above package (122–50 cm) corresponds to laminated sandy silt with some interbedded layers of bioclastic gravel-sized fragments. The top of this package displays a sharp contact due to dredging activities in the area, and the upper section of the core (50–0 cm) corresponds to the most recent sedimentation of seismic unit U7, characterized by dark bioturbated sandy silt.

4.3. Pollen analyses

The synthesis of the main results presented for each section studied includes the main pollen and NPP percentages (Fig. 5A, 6A, 7A and 8A) and concentrations (Fig. 5B, 6B, 7B and 8B), and the absolute abundances of the main dinoflagellate cysts types (Fig. 5C, 6C and 7C).

VC7 (60–220 cm) The 21 samples studied extent from before 10,200 to after 8500 cal yr BP, and can be divided in three main LPAZs, some of them also including subzones (Fig. 5).

LPAZ-1: This is the local pollen zone with the lowest concentration of palynomorphs of this section. Total tree pollen (AP) is consistently low in this zone, which is dominated by Poaceae, Compositae (Tubuliflorae,

Liguliflorae) and cf. *Juncus*. Main tree types include conifers (*Pinus* and *Juniperus*) and riparian taxa (*Salix, Alnus*). Subzone LPAZ-1b is characterized by increasing evidence of heath (*Erica*), aquatics/hygrophilous (*Ranunculus-type*) and *Quercus*.

LPAZ-2: It is characterized by the retreat of cf. *Juncus* and the progressive decline of fungal remains. Besides, AP values increase due to the successive expansions of *Quercus* (LPAZ-2a) and *Corylus* (LPAZ-2b), and reflects the occurrence of *Carpinus*. *Ranunculus-type* also peaks in subzone LPAZ-2b. In addition, this zone also includes almost continuous presences of *Ruppia* and greater concentrations of dinoflagellate cysts than the previous zone.

LPAZ-3: It represents a new increase of *Quercus* and decline of *Corylus*, with new maxima of Compositae (Liguliflorae, Tubuliflorae), cf. *Juncus, Juniperus, Ruppia*, foraminiferal linings and dinoflagellate cysts.

GC2X (200–285 cm) Most of the levels analysed in this sequence are older than 8000 cal yr BP and have noticeable concentrations of palynomorphs, particularly pollen. The 14 samples studied can be divided into three LPAZs (Fig. 6).

LPAZ-1: This zone represents the maximum development of *Pinus, Juniperus, Erica*, Poaceae, Compositae (Tubuliflorae and Liguliflorae) and cf. *Juncus*.

LPAZ-2: It is characterized by the highest AP values due to the rising of the deciduous trees (*Corylus, Quercus*) with also the presence of *Carpinus*. *Ruppia* appears in this zone, where also a minor increase in
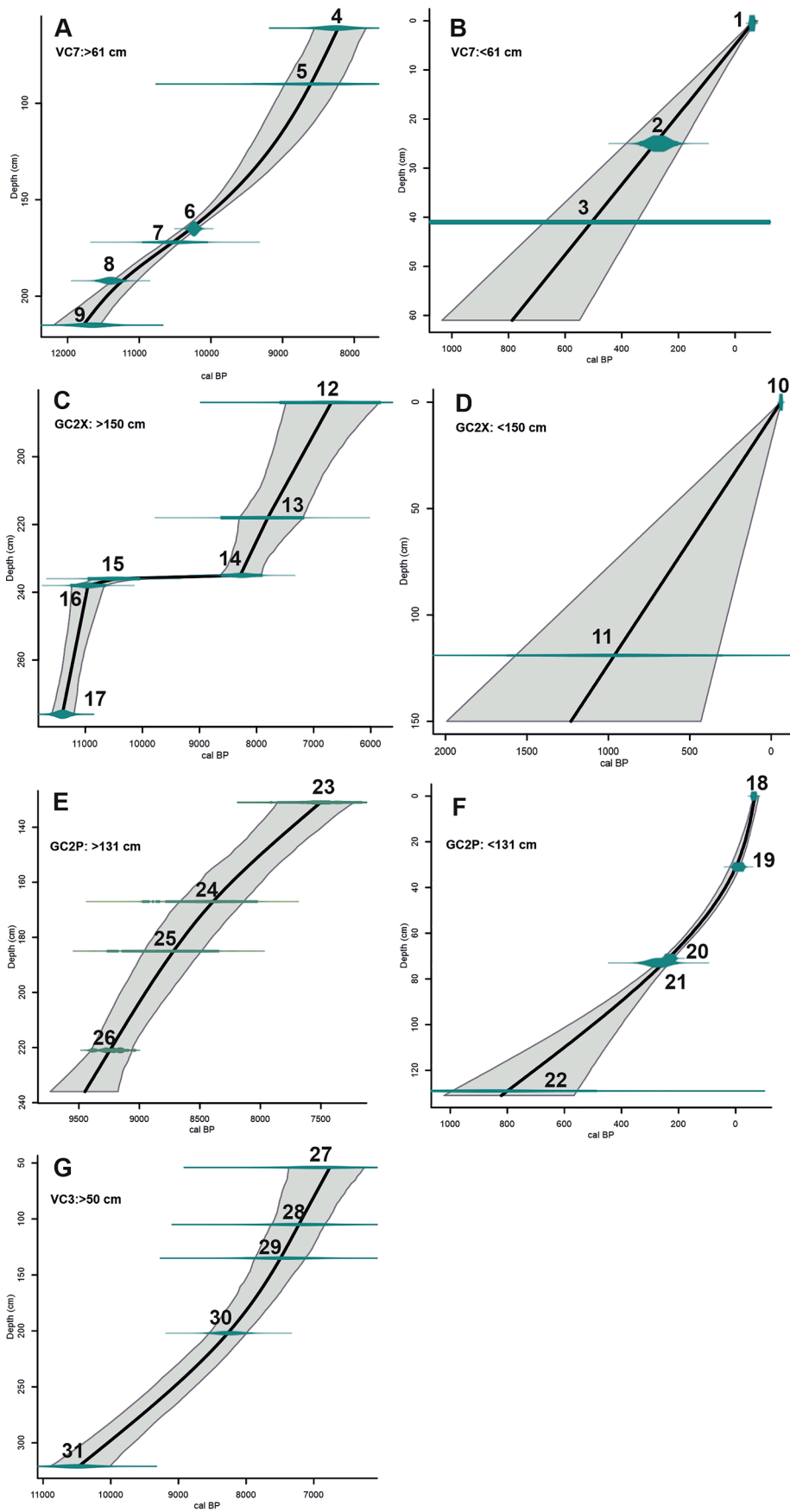
Fig. 4. Age-depth models adopted for all the sections studied (Fig. 5,6,7 and 8). They have been performed with CLAM 2.3.2 (Blaauw, 2010). Curves A, E, F and G have been produced using the smooth-spline method (smoothing level 0.3, Blaauw, 2010); and the others (B, C and D) using the polynomial regression approach. Numbers indicate the chronological benchmarks showed in the Table 3. No age-depth model has been performed for the top of VC3 (0–50 cm) because the dredging activities in the area (see the text).

CORE **VC7**, *Ría de Ferrol* (-18.8 m NMMA)
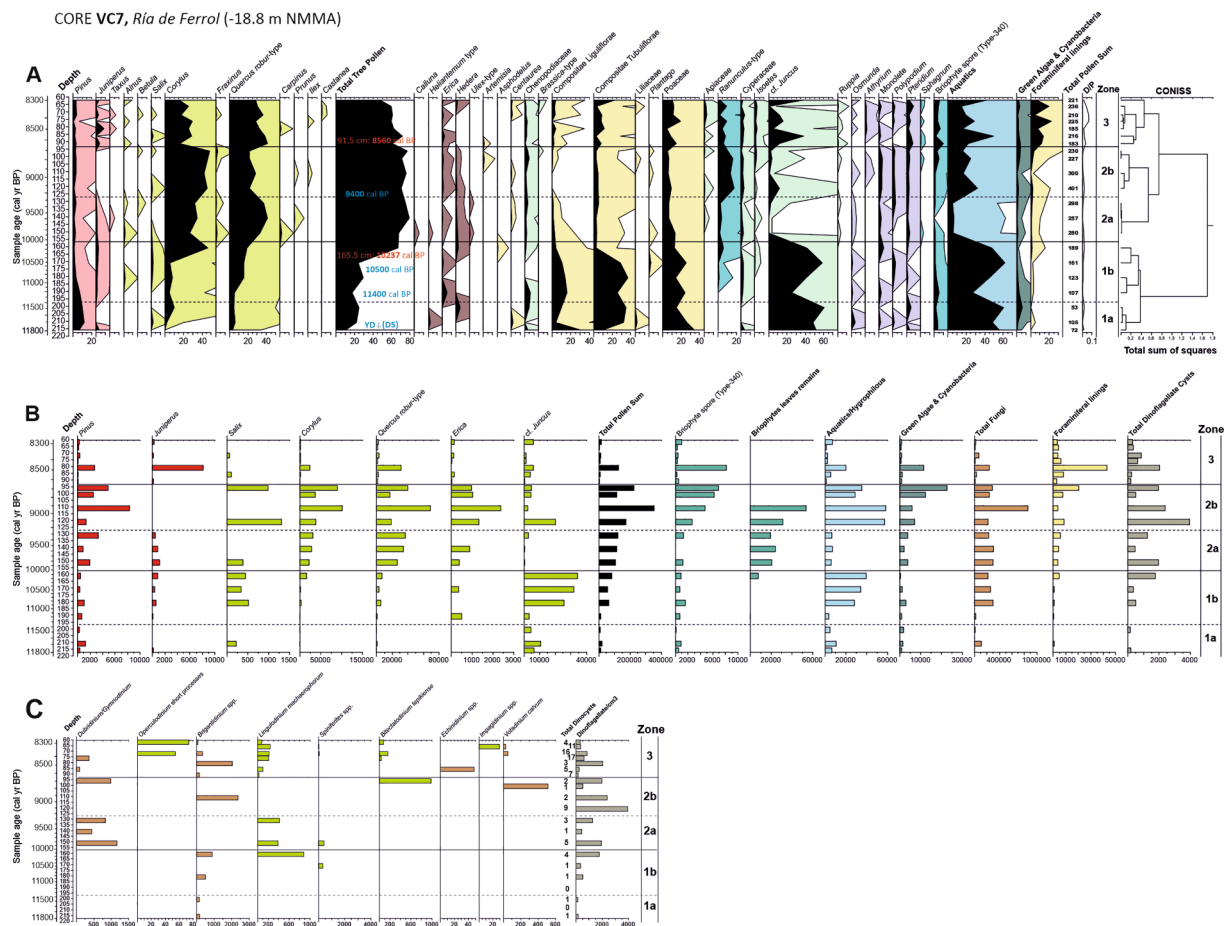
Fig. 5. Summarized pollen data from core VC7, Ría de Ferrol (-18.8 m NMMA). (A) Diagram of percentages for the main pollen and NPP types, including D/P ratios and CONISS analysis. (B) Diagram of diagram absolute abundances (grains/g) for selected pollen and NPP types. (C) Diagram of absolute abundances (cyst/g) of the main types of dinoflagellate cysts identified. Chronological framework: [14]C data (red) and other chronological inferences obtained by correlation between data and other environmental evidence (blue) are showed. See the text.

dinoflagellate cysts is recorded.

LPAZ-3: It represents the maximum development of *Quercus* and *Ranunculus-type*, with the continuous presence of *Salix* and increasing evidence of foraminiferal linings and dinoflagellate cysts.

GC2P (0–236 cm) As many as five different LPAZs were identified in this core that records something further than the last 8 kyrs of environmental history in the basin (Fig. 7). Useful abundances of palynomorphs have been found in most of the levels studied (with the exception of the sample 230 cm deep that resulted very poor in organic microremains and most of them are fungal materials, see Fig. 7ABC), but concentrations of dinoflagellate cysts strongly oscillate between zones, being high in LPAZ-5, LPAZ-4 and LPAZ-1, noticeable lower in LPAZ-3, and poor or very poor in most of the samples included in LPAZ-2 (Fig. 7C). Below are described the main characteristics of each pollen zone.

LPAZ-1: Only two samples are included in this zone, but they are consistently similar between them and very different to the group of samples above. These two levels are rich in pollen, fungal remains and dinoflagellate cysts, with noticeable values (60%) of AP, mainly deciduous (*Quercus, Corylus, Betula*) and riparian trees (*Alnus, Salix*), but also heath (*Erica*) and freshwater/hygrophilous (*Ranunculus*-type, *Equisetum*) and brackish/marine (Chenopodiaceae, *Ruppia*) taxa.

LPAZ-2: Both the pollen and fungal remains concentrations notably decrease in this zone. Besides, both *Ruppia* and Chenopodiaceae disappear, and also the abundance of dinoflagellate cysts in the sediment becomes scarce or null. Deciduous trees notably retreat, but *Pinus*, herbs (Poaceae, Compositae Tubuliflorae, Compositae Liguliflorae) and

aquatics/hygrophilous (Cyperaceae, cf. *Juncus, Equisetum, Potamogeton/ Triglochin*, green algae and cyanobacteria) increase.

LPAZ-3: Total remains concentration notably increases, especially pollen and fungal remains. Besides, also the occurrence of dinoflagellate cysts almost constantly rises in this zone. AP increases in subzone LPAZ-3a, with maximum development of *Quercus,* and also *Corylus* and *Betula* rising, but *Pinus* retreating. Furthermore, *Ruppia* and Chenopodiaceae also reappear here. *Corylus* peaks in the subsequent LPAZ3b subzone, where AP reaches its maximum percentages in the complete GC2P sequence.

LPAZ-4: This entire zone is characterized by the AP retreat, mainly *Corylus, Quercus* and *Pinus*. Alternatively, heaths (*Erica*), herbs (Poaceae, Compositae Tubuliflorae, Compositae Liguliflorae) and some aquatics/ hygrophilous (Cyperaceae, cf. *Juncus*) increase. However, another group of aquatics/hygrophilous, including freshwater (*Ranunculus-type*) and brackish/salty (Chenopodiaceae) taxa, retreats. Two different subzones may be differentiated: LPAZ-4a, characterized by the maximum development of *Alnus* and *Betula* in the sequence but also by the apparition of *Castanea;* and the subzone LPAZ-4b, which includes a decline of *Alnus* and peaks of *Castanea, Erica* and Poaceae, but also the beginning of the *Olea* pollen curve. Otherwise, the abundances of dinoflagellate cysts and foraminiferal linings noticeably increase in LPAZ-4.

LPAZ-5: AP increases again sharply related to the modern afforestation with *Pinus* and *Eucalyptus*. Besides, new increases in *Ranunculus-type* and Chenopodiaceae and consistently high abundances of dinoflagellate cysts are observed.

VC3 (160–325 cm) The concentration of palynomorphs is low or
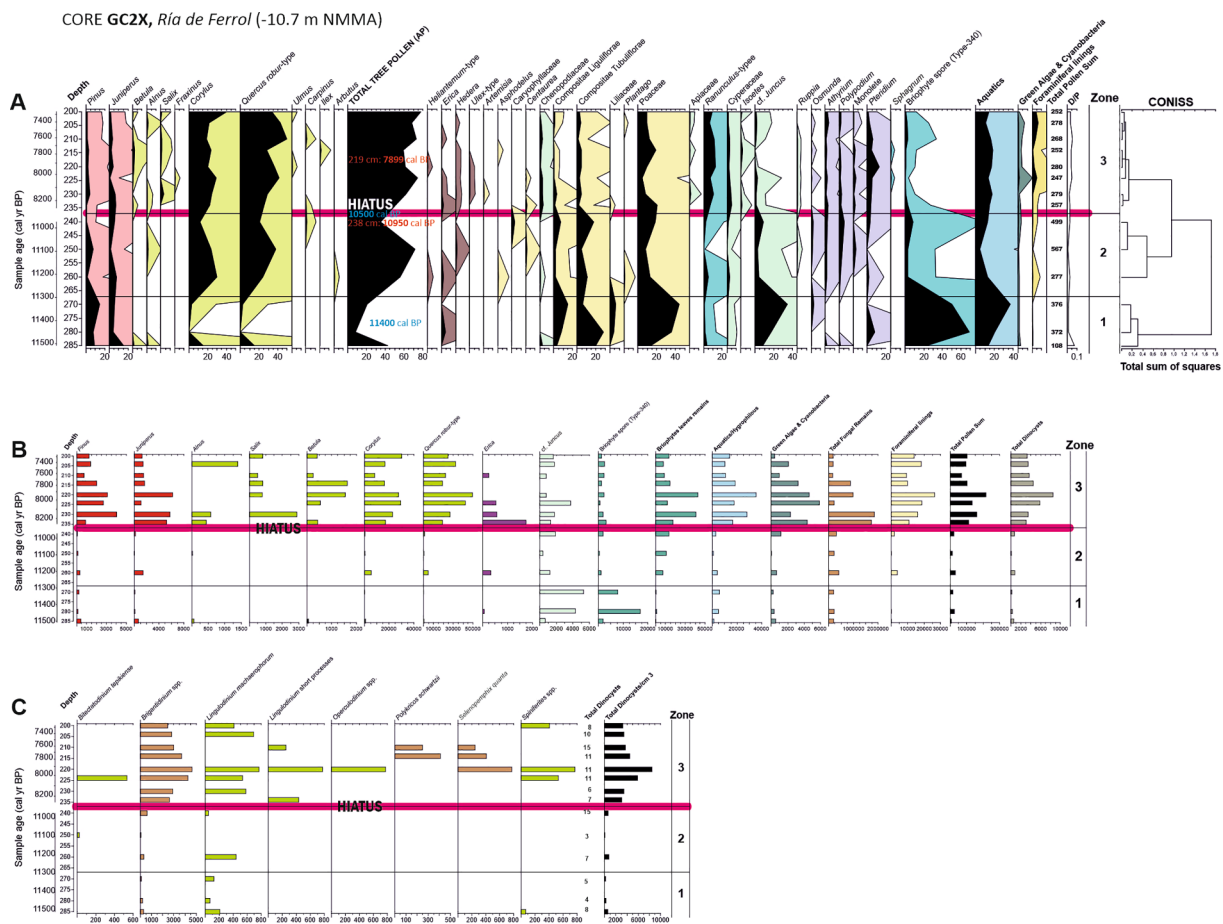
Fig. 6. Summarized pollen data from core GC2X, Ría de Ferrol (-10.7 m NMMA). (A) Diagram of percentages for the main pollen and NPP types, including D/P ratios and CONISS analysis. (B) Diagram of diagram absolute abundances (grains/g) for selected pollen and NPP types. (C) Diagram of absolute abundances (cyst/g) of the main types of dinoflagellate cysts identified. Chronological framework: ¹⁴C data (red) and chronological inferences obtained by correlation between data and other environmental evidence (blue) are showed. See the text.

very low in most of the levels analysed in this section (Fig. 8). The two LPAZs identified are dominated by cf. *Juncus* and have been dated as older than 7470 cal yr BP (Table 2). Nevertheless, maximum development of *Pinus*, Cyperaceae and Compositae Tubuliflorae occurs in zone LPAZ-2. Besides, evidence of foraminiferal linings and dinoflagellate cysts only occurs at the top of this section.

4.4. XRF-Analysis

Main results useful for environmental inferences can be summarized as a reduced number of elemental parameters (S, Br, Ca) and ratios (Ti/Ca, Br/Cl, K/Ti, Zr/Rb) represented in Fig. 9. These selected data are geochemical evidence related to the changing marine/terrestrial influences recorded in each site cored. In each case, complete XRF results (represented as counts) are showed (red points), but trends are more adequately interpreted according to the running average of 20 data (blue curves). In order to clarify the discussion below, these data are directly compared with some selected pollen curves (percentages, concentrations and D/P ratios) that can support our ecological reconstructions and chronological inferences.

5. Discussion

5.1. Discontinuities and ages estimated for the sedimentary sections studied

The upper 50 cm in core VC3 are affected by modern dredging

activities and, therefore, considered useless for environmental inferences. Besides, the seismic discontinuity D6 has been identified in cores VC7, GC2X and GC2P, respectively, at ca. 60, ca. 150 and ca. 130 cm (Fig. 3). Thus, these three sequences present notable hiatuses extending from the middle Holocene to the historical period. Age-depth models (Fig. 4) performed upon the chronological benchmarks in Table 3 indicate that the age of the VC7 sediment > 61 cm extends between ca. 12000–8300 cal yr BP; the GC2X section > 150 cm ranges between ca. 11500–7300 cal yr BP; and the GC2P section > 131 cm between ca. 8400 and 6600 cal yr BP. Chronology of the upper 131 cm of GC2P and the upper 61 cm in VC7 may be relatively precisely dated to be younger than ca. 800 cal yr BP. The age model for the < 131 cm section in GC2X is imprecise, but probably covers the last 1200 cal yr BP. Finally, the VC7 record > 50 cm extents between ca. 10,400 and 7000 cal yr BP (Fig. 4).

5.2. Pollen evidence of Juncus representing high marshes or ephemeral coastal ponds

Juncus spp. is a common component of coastal marshes everywhere and also in NW Iberia, where is forming part of high marshes, ephemeral coastal plain ponds (oxbows and pond shores) or humid dune slacks (e.g. Evans, 2006; Houston, 2008; Muñoz Sobrino et al., 2016). Nevertheless, Juncaceae are frequently infra-represented in surface pollen assemblages due to the pollen degradation (e.g. Bunting, 2003; Amami et al., 2010; García-Moreiras et al., 2015; Waller et al., 2017). Faegri and Iversen (1964) describe the *Juncus* pollen as psilate, inaperturate pollen

CORE **GC2P**, *Ría de Ferrol* (-10.5 m NMMA)
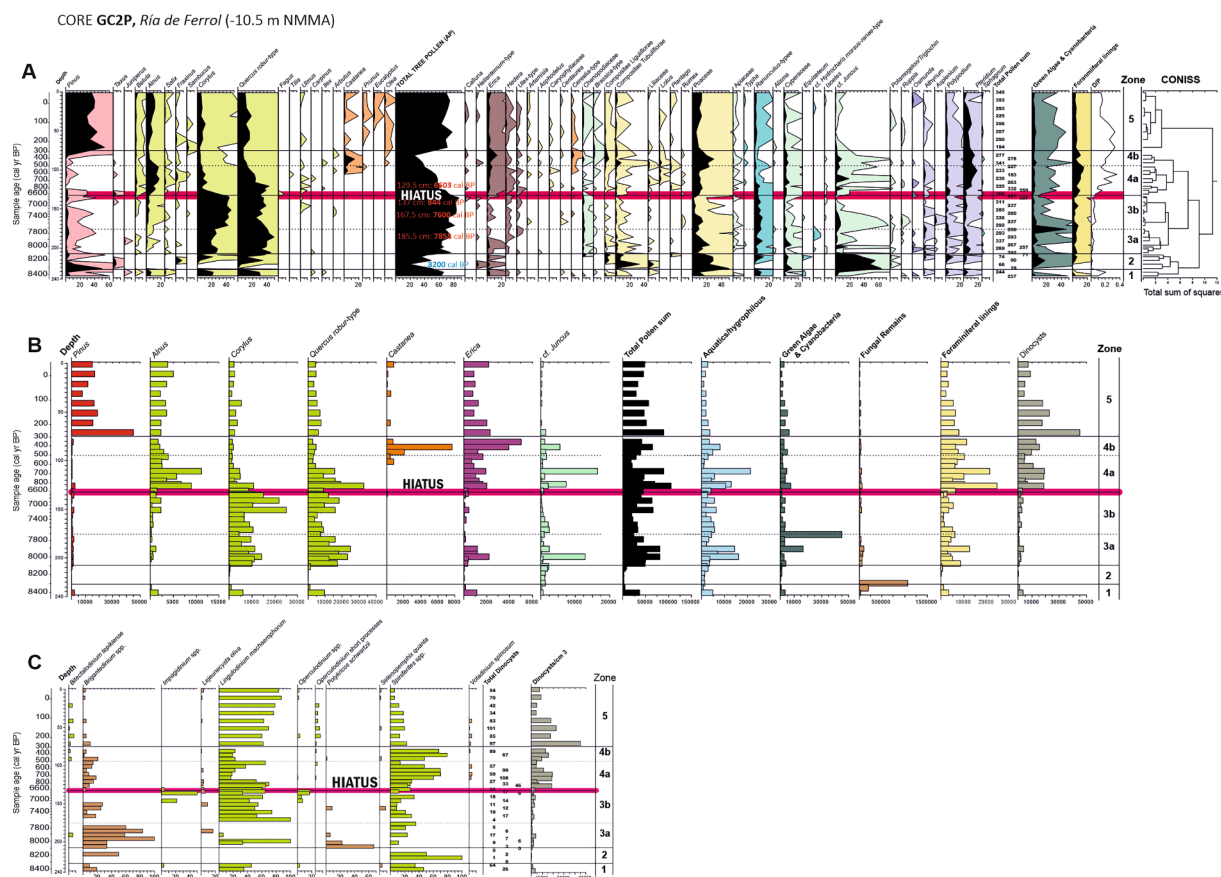
Fig. 7. Summarized pollen data from core GC2P, Ría de Ferrol (-10.5 m NMMA). (A) Diagram of percentages for the main pollen and NPP types, including D/P ratios and CONISS analysis. (B) Diagram of diagram absolute abundances (grains/g) for selected pollen and NPP types. (C) Diagram of absolute abundances (cyst/g) of the main types of dinoflagellate cysts identified. Chronological framework: [14]C data (red) and chronological inferences obtained by correlation between data and other environmental evidence (blue) are showed. See the text.

grains united in tetrad; and with exine extremely thin because it is typically not preserved in fossil state or at any rate not recognized. Besides, acetolysis can damage or destroy Juncaceae pollen (Erdtman, 1952; van Asperen et al., 2016). In addition, the usually very crumpled pollen of sub-fossil Juncaceae can be often mistaken for thin-walled Cyperaceae (e.g. Fredskild, 1970). Thus, palaeoecological evidence of *Juncus* sedges is more frequently demonstrated by carpological/macro-fossil remains but not by pollen data (e.g. Di Rita et al., 2016). Nevertheless, certain *Juncus* environments may be eventually distinguishable by the abundance of other types of palynomorphs, mainly fungal remains (e.g. Marsh and Cohen, 2008; Muñoz Sobrino et al., 2014; García-Moreiras et al., 2015).

In the RdF, high percentages and concentrations of a palynomorph that tentatively was identified as cf. *Juncus* has been found at different depths in the four sections of sediment analysed. The most significant concentrations of cf. *Juncus* (more than 10^4 grains/g) have been found between 75 and 130 cm in GC2P (Figs. 7B and 9C). Likewise, concentrations of more than 5×10^3 grains/g of sediment appear in VC3 at 160 cm and below 255 cm (Figs. 8B and 9D). Finally, pollen peaks of cf. *Juncus* (between 2 and 5×10^3 grains/g) also resulted at 120 cm and between 160 and 180 cm in VC7 (Figs. 5B and 9A), and between 225 and 240 cm and below 275 cm in GC2X (Figs. 6B and 9).

This type of pollen remain has been identified in different samples as groups of tetrads, tetrads, groups of 2–3 grains or isolated grains (Fig. 10), but pollen counts obtained correspond to individual grains in all the cases. In order to confirm the pollen identification, some fresh pollen material corresponding to *Juncus maritimus* Lam. was recollected in a high marsh from Ría de Vigo (García-Moreiras et al., 2015) and subjected to the same treatment as the sediment samples analysed (acid

HCl + HF treatment, without acetolysis). Comparative image analyses of the remains resulted (Fig. 10) reinforce our identification of the cf. *Juncus* microremains as pollen evidence of the local occurrence of Juncaceae, likely *J. maritimus* Lam, *J. gerardii* Loisel. or *Juncus acutus* L., the most abundant species on the Galician coasts (Asensi and Diez-Garretas, 2017).

Reasons that explain these unusual *Juncus* pollen abundances on the studied sediments may be not only related to the chemical treatment applied (HCl + HF, without acetolysis) but also to the high local abundance of *Juncus* sp. in the original ecosystems (*Juncus* may be almost monospecific on high-marsh patches, shores of ephemeral coastal ponds and humid dune slacks), the presumably rapid burial of most of these levels, which may be connected with the rapid rise of RSL (see discussion below), and the exceptional conditions for pollen preservation of this type of sediment: anoxic environments with abundant organic carbon supply as revealed the high S contents (Fig. 9; e.g. Wasmind et al., 2017; Wiessner et al., 2010, 2017) and Br/Cl ratios (Fig. 9; e.g. Gerritse and George, 1988).

5.3. Environmental and chronological inferences derived from XRF and pollen data

Pollen and XRF data complement each other, aiding in a more detailed environmental reconstruction when the trends in elemental data match changes in the pollen successions and can be interpreted as the consequence of environmental processes. It has been previously demonstrated that different chemical forms of sulphur (S) are transformed and abundantly deposited in the Juncaceae/Poaceae rhizosphere of coastal salt marshes and that the accumulation of organic

CORE **VC3**, *Ría de Ferrol* (-10.3 m NMMA)
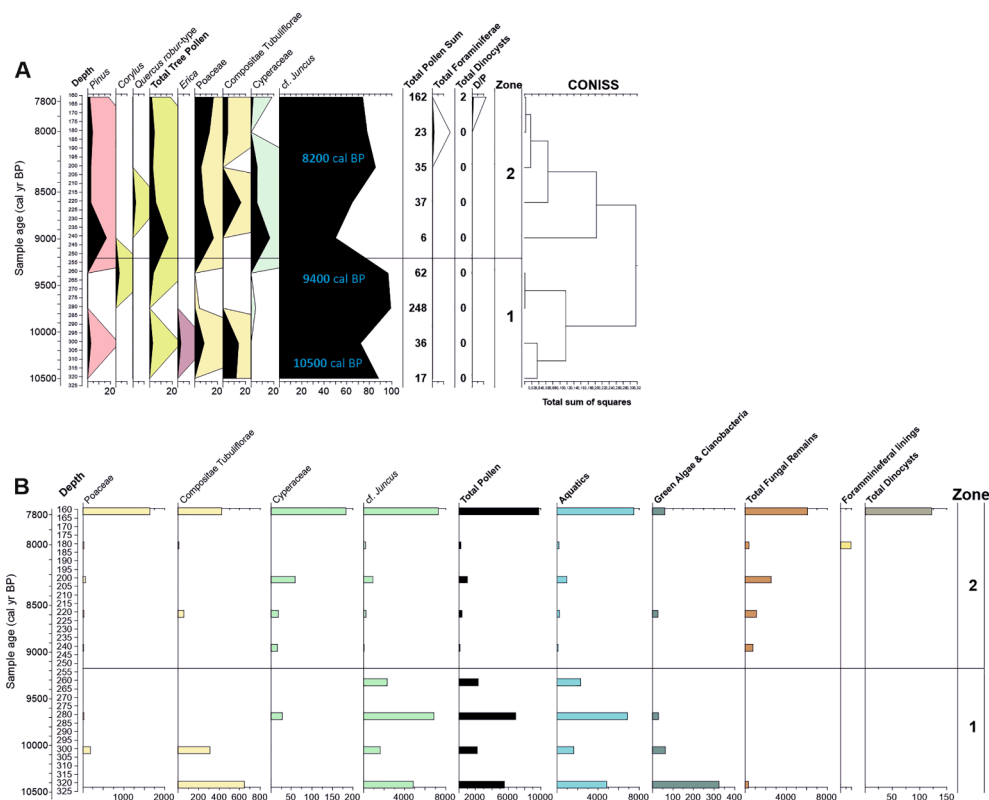
Fig. 8. Summarized pollen data from core VC3, Ría de Ferrol (-10.3 m NMMA). (A) Diagram of percentages for the main pollen and NPP types, including D/P ratios and CONISS analysis. (B) Diagram of diagram absolute abundances (grains/g) for selected pollen and NPP types. Chronological framework: [14]C data (red) and chronological inferences obtained by correlation between data and other environmental evidence (blue) are showed. See the text.

matter contributes to the immobilization of that S (Ferdelman et al., 1991; Wiessner et al., 2017). In addition, the interaction of the water level and salinity had a significant effect on both the total S content and the C/S ratio, so that higher total S contents appear in surface soils under moderate salinity and low water levels (Lu et al., 2016), which may be assumed the typical conditions of the high marshes (García-Moreiras et al., 2015). Additionally, S formation and preservation is enhanced in the upper marsh sediment, where inorganic sulphur compounds are rapidly oxidized (Ferdelman et al., 1991). Besides, the bromide (Br) temporal variability may reflect its close relationship with sediment organic matter and alterations in Br biogeochemical recycling in marsh environments. Previous studies in marshes on the Iberian Atlantic margin indicate that the highest Br enrichment in modern sediments was found during the Maunder Solar Minimum (CE 1645–1715; ca. 270 cal yr BP), a major solar event (Dorman, 2016) characterized by lower irradiance and temperatures, and increasing cloudiness and albedo. This suggests that climate-induced changes weaken the natural mechanisms that promote Br biochemical transformations, mainly driven by both living plants metabolism and plant litter degradation, and minimize the generation of volatile CH_3Br during the cold periods (Moreno et al., 2015). The calcium (Ca) content usually reflects changes in biogenic calcium carbonate production (Gebregiorgis et al., 2020) that may be related to increasing marine influence (i.e. regional changes in the sea level).

Concerning the different ratios presented (Fig. 9), high Ti/Ca values indicate greater influence of terrigenous material (Rothwell and Croudace, 2015), high Br/Cl values point to high concentrations of organic matter (Rothwell and Croudace, 2015, Cartelle et al., 2019), and high Zr/Rb indicates less amount of clay and enrichment in coarse grains (Rothwell and Croudace, 2015). Finally, the K/Ti proxy has been demonstrated to be applicable to the coast of Galicia and can indicate

the relative influence of fluvial or local sediment contributions (Arribas et al., 2010; Cartelle et al., 2019). When the K/Ti value is low, there is a greater contribution of fresh eroded material transported by rivers, but as the value increases, it indicates a greater contribution of recycled material from the surroundings (coastal erosion, predation of old deposits, etc).

Our results reveal that cores GC2X and CG2P showed similar facies succession and lithologies (Fig. 3) and, accordingly, most of the elemental data trends observed are almost the same, but certain differences also exist (Fig. 9). Maxima S values appear between 230 and 250 cm in GC2X and between 198 and 210 cm in GC2P (Fig. 9). In both cases, those levels also show increasing Br values and therefore are interpreted as colder stages during which the amount of organic matter preserved in the sediment increased. Below, grey (gleyed) sediments exist in both cases, characterized by high Ti/Ca values that denote high terrigenous influences. However, a peak in Zr/Rb (coarser materials) appears at the base of GC2P that cannot be identified in GC2X. Instead, the last show an increase of Chenopodiaceae not recorded in the former. Those differences are probably the result of the core GC2X being more influenced by tidal processes than the core GC2P, which is 36 m distant (Fig. 2B) and whose base is located about 20 cm above the GC2X base. All these XRF evidence, combined with pollen data (Fig. 9; see discussion below), suggest that between ca. 10950–7900 cal yr BP high marshes developed in these points that at that time were situated below −12.5/-13.1 m NMMA. Marine influence (low Ti/Ca) increases in both sequences from ca. 7900 cal yr BP; but, again, their relative altitude differences can explain that the biogenic Ca contribution was higher in the first (GC2X), at least until before ca. 6700 cal yr BP (Fig. 9B). Finally, a conspicuous Br peak (also denoted by the anomalous Br/Cl peak) can be observed at 73 cm in GC2P (Fig. 9C), which probably corresponds with a minor increase at 107 cm in GC2X (Fig. 9B). Then, it can be assumed that the prevailing
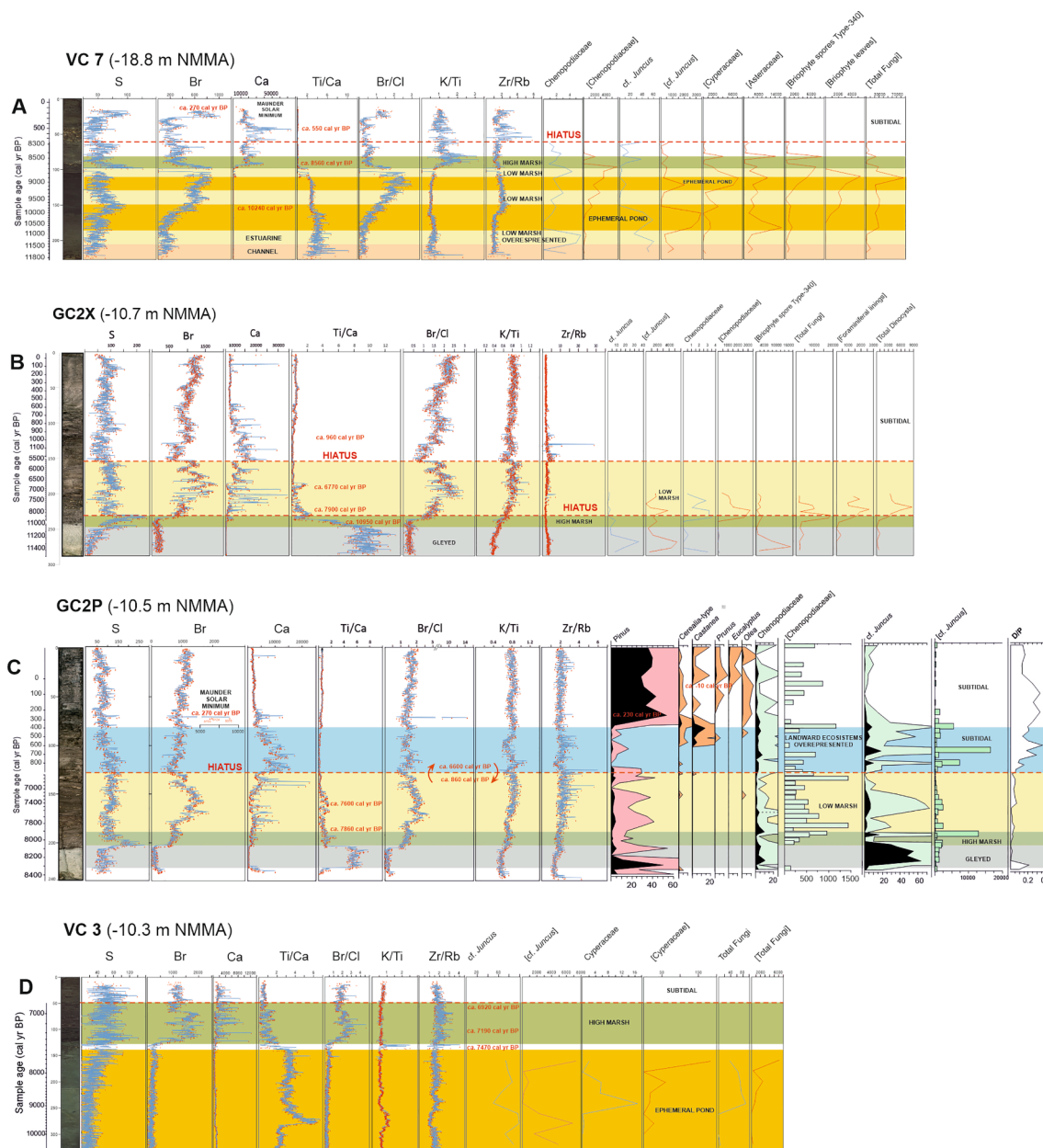
Fig. 9. Main elemental (X-ray fluorescence) results compared to selected pollen evidence for the different cores discussed, including chronological evidence and environmental interpretations (see the text). (A) VC7; (B) CG2X; (C) CG2P and (D) VC3.

climate conditions during the Maunder Solar Minimum (ca. 270 yr BP) favoured the retention of more Br in marsh ecosystems, ultimately decreasing the biogenic Br emissions to the atmosphere. The chronology of this event may also be supported by the beginning of the regional repopulation with pines observed in the complete GC2P pollen sequence (Figs. 7 and 9C), an event that in this region began after ca. 230 cal yr BP (Table 3).

In the shallowest VC3 core (Fig. 9D), the greatest terrigenous contribution (high Ti/Ca values) is registered before ca. 7470 cal yr BP, when indicators of organic matter remain low (S, Br, Br/Cl). At ca.7470 cal yr BP conspicuous peaks of K/Ti and Zr/Rb reveal increasing coastal erosion, with enrichment in coarse materials that may be mainly of non-biogenic origin as the Ti/Ca ratio remains high (Fig. 9D). Later, S, Br, and Br/Cl notably increase from ca. 7470 cal yr BP until younger than 6920 cal yr BP, while Ca values remain relatively low. These trends are comparable to those recorded in the high marsh levels described in GC2X and GC2P (Fig. 9BC). Recent dredging activities in the ria

truncated the top of core VC3 and, therefore, the upper 50 cm correspond to recent deposition (less than 20 years, Fig. 3).

In the deepest VC7 core, Ti/Ca ratios registered below 200 cm are comparable to those of the base (<135 cm) of VC3 (Fig. 9). Besides, organic matter indicators (S, Br, Br/Cl) also remain low, only increasing from 180 cm upwards, with the first peak at 150 cm that can be locally dated at ca. 10240 cal yr BP (Fig. 9A). Nevertheless, the highest S values appear at 100 cm, dated at ca. 8560 cal yr BP, preceding a notable increase in Ca (revealing the sea-level rise) and a new K/Ti peak indicating the erosion of old coastal deposits by the rising sea. Most probably, these peaks of Ca and K/Ti may correspond to those dated at ca. 7470 cal yr BP in VC3 (Fig. 9D). At ca. 60 cm, a peak of Zr/Rb denotes an increase of coarse grains that signal the seismic discontinuity D6. Above it, the maximum of Ca has been locally dated at ca. 550 cal yr BP. Therefore, the Br maximum observed about 27 cm may be consistently interpreted as local evidence of the Maunder Minimum (Fig. 9A).
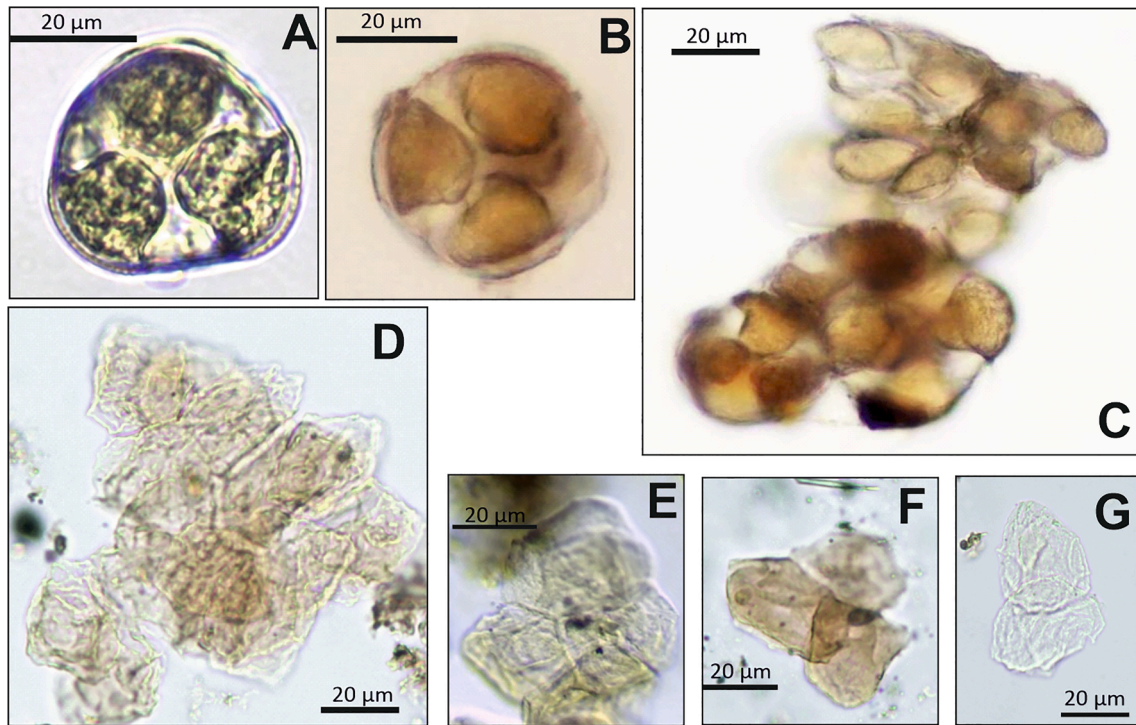
Fig. 10. Comparative image analyses of fresh *Juncus maritimus* Lam. pollen material (A), fresh pollen material after acid HCl + HF treatment without acetolysis (B and C) and different subfossil evidence found in RdF as groups of tetrads (D), tetrads (E) or groups of 2–3 grains or isolated grains (F, G).
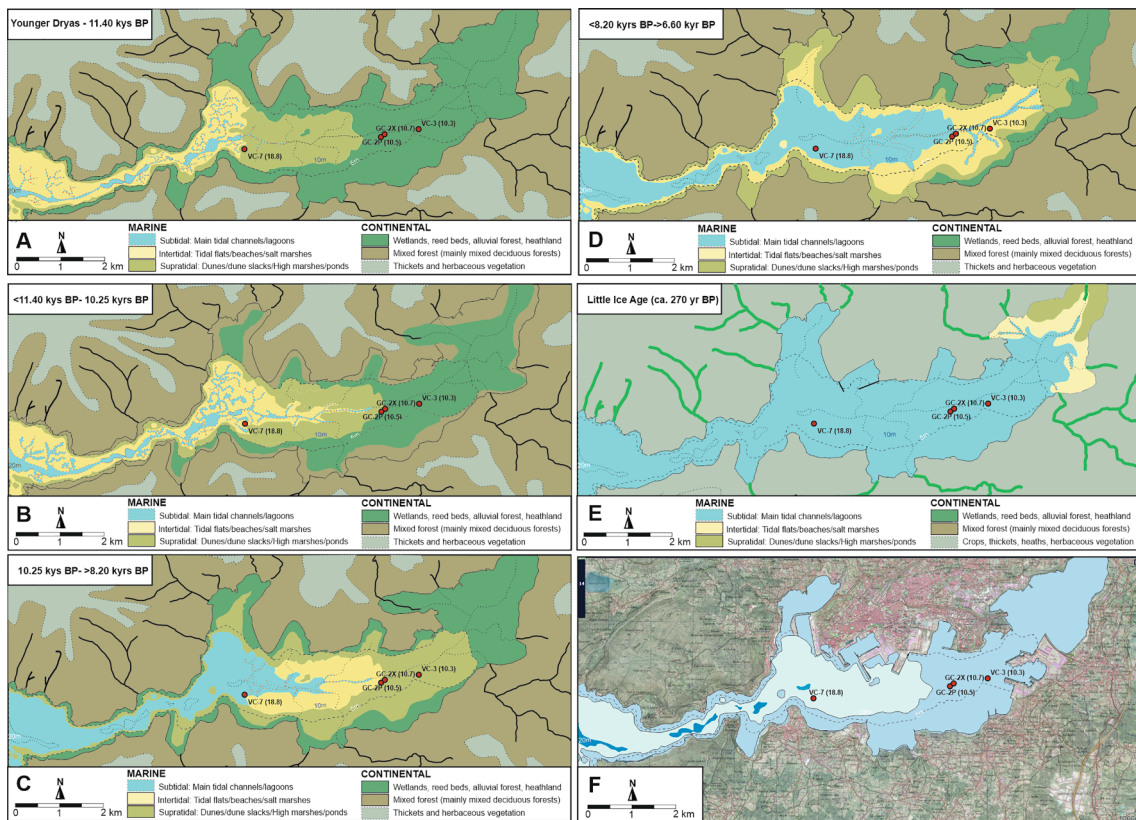
Fig. 11. Spatial-temporal changes reconstructed in the innermost part of Ría de Ferrol upon the multiproxy analyses presented in this study. (A) Period comprised between the Younger Dryas and 11400 cal yr BP; (B) Between later than 11,400 to 10,250 ca. yr BP; (C) Between 10,250 ca. yr BP and before 8200 cal yr BP; (D) Between after 8200 cal yr BP and before 6600 cal yr BP; (E) during the Little Ice Age (ca. 270 cal yr BP); (F) Modern configuration of Ría de Ferrol.

5.4. Spatial-temporal changes of local ecosystems by fluctuating terrestrial/marine influences

The deepest levels of VC7 (>215 cm, at the base of the seismic unit U6 and close to discontinuity D5) represent a visible change in the sedimentation (Figs. 3, 5 and 9A) and might be tentatively interpreted as the latest stages of the Younger Dryas (YD; 12730–11650 cal yr BP), the strongest climate reversal recorded in NW Iberia after the last glacial maximum (Muñoz Sobrino et al., 2001; Iriarte-Chiapusso et al., 2016). After this, the multiproxy data collected suggest the local occurrence of a channel hardly influenced by tides and the development of coastal emerged plains, dunes and other associated ecosystems close to the location of VC7. Therefore, and before beginning to rise at ca. 11650 cal yr BP, the RSL in the RdF would be located well below −21 m NMMA. Above that basal levels, the fining upwards succession recorded in the core indicates a progressive reduction in energetic conditions (channel abandonment sequence, Fig. 3), a likely consequence of the base-level rise. Between 215 and 170 cm VC7 sequence includes two stages dated before 10240 cal yr BP, characterized by conspicuous peaks of cf. *Juncus* and Compositae, and separated by another phase of increases in heaths and Chenopodiaceae (Fig. 5). Therefore, they should be most probably related to two minor cold reversals (with the subsequent stabilization of the sea level rise) occurring between the YD and the Early Holocene level dated at ca. 10240 cal yr BP, presumably the 11.4 and 10.5 cal kyr cold events that have been previously described in other coastal areas from NW Iberia (García-Moreiras et al., 2019b).

According to this interpretation, before 10950 cal yr BP, the marine pollen evidence (dinoflagellate cyst, foraminiferal linings) is still very low in CG2X (Figs. 6 and 9B) and low in VC7 (Figs. 5 and 9A). Nevertheless, Chenopodiaceae pollen found at both sites (but more abundant in VC7) may also indicate the occurrence of channels that were eventually influenced by high/spring tides (MHWST), particularly during an apparently warmer stage observed between the YD (not recorded in CG2X) and the 11.4 kyr event (Fig. 11). Meanwhile, core GC2X recovers sediment from the inner estuary, where seismic and sedimentary data point to the existence of extensive floodplains (Figs. 2 and 3). High pollen percentages (but low pollen concentrations) of Compositae, Poaceae, Liliaceae, etc, suggest the development of nearby dune ecosystems on the coastal lowlands (e.g. Muñoz Sobrino et al., 2016). The expansion of total tree pollen (AP) percentages dated before 10950 cal yr BP in CG2X coincides with the increasing evidence of foraminiferal remains (Figs. 6 and 9B). Noticeably, that tree pollen increase precedes the AP expansion observed in VC7 (<10240 cal yr BP, Figs. 5 and 9A), probably because the CG2X site is placed higher than VC7, closer to the main tree pollen sources (Fig. 1C).

During the period interpreted as the 11.4 kyr event, very strong evidence (high concentrations) of mosses remains and other freshwater/hygrophilous vegetation (*Ranunculus*-type) exist in CG2X but not in VC7 (Fig. 9AB). Besides, that stage passes without any evident tidal influence being recorded at CG2X (e.g. lack of Chenopodiaceae, high Ti/Ca and low K/Ti ratios). Those data indicate a sea-level position below the point CG2X and the local development on the emerged lowlands of grey dunes, intra-dune depressions (dune slacks) or coastal freshwater wetlands (Fig. 11).

After a new period (ca. 11400–10950 cal yr BP) of stronger marine influence (with the presence of *Ruppia* and increasing evidence of foraminiferal linings in CG2X), there is a second stage of stabilization in both sequences, most probably dated at ca. 10500 yr BP, because it is younger than 10950 yr BP in GC2X but older than 10240 yr BP in VC7 (Figs. 4, 6 and 9). In CG2X, this stage is characterized by the absence of Chenopodiaceae and minor new increases of cf. *Juncus*, Compositae, Poaceae and bryophyte remains (Fig. 6). In VC7, it is represented by a second conspicuous peak of cf. *Juncus*, Compositae and Poaceae, increases of other aquatics/hygrophilous (Cyperaceae, *Ranunculus*-type, *Isoëtes*) and the decrease of Chenopodiaceae (Fig. 4); all of them suggesting lower marine influence at the two points discussed (Fig. 11).

Marine evidence progressively increases after 10240 cal yr BP in VC7 (e.g. apparition of *Ruppia* and increase of foraminiferal abundance), and the highest local representation of dinoflagellate cyst and foraminiferal linings is reached at this site after 8560 cal yr BP (Fig. 5). Nevertheless, a new increase of heaths (*Erica*), cf. *Juncus, Ranunculus*-type, and bryophyte remains also appear at ca. 125 cm in this sequence. That rise of freshwater vegetation is simultaneous to the decrease in marine indicators (*Ruppia*, foraminiferal linings, dinoflagellate cyst). Upon the radiocarbon dates available, it is possible to calculate an interpolated age of ca. 9430 yr BP for this phase, suggesting that it can be related to another minor cold event (the 9.3 event) just previously described in other very sensitive continental (Iriarte-Chiapusso et al., 2016) and marine sequences (García-Moreiras et al., 2019a) from NW Iberia.

Later than 8560 cal yr BP the sequence VC7 (Fig. 5) indicates a last increase of marsh (cf. *Juncus*, Cyperaceae, *Isoëtes*) and dune (Compositae, *Juniperus*, *Artemisia*, *Pteridium*, bryophytes) vegetation. Meanwhile, marine indicators also persist at this site (*Ruppia*, dinoflagellate cysts, foraminiferal linings, Chenopodiaceae, high K/Ti ratio). This pollen and XRF evidence agrees with that observed at the base of core GP2P (and dated earlier than 7860 cal yr BP; see Fig. 7), and jointly may be connected with the more prominent cold episode described in NW Iberia during the Early Holocene, the 8.2 kyr event, which pollen signal is particularly strong in peatbogs placed at the nearby Cantabrian Mountains (Fig. 1A; Muñoz Sobrino et al., 2005, 2007; Iriarte-Chiapusso et al., 2016). Besides, it also has been identified in other fluviomarine systems from NW Iberia (García-Moreiras et al., 2019a). Nevertheless, this stage is not apparent in the sequence CG2X (Fig. 6), surely because it includes a hiatus (Figs. 4, 6, 9) extending from later the beginning of the 10.5 kyr event (<10950 cal yr BP dated at 240 cm) to after the end of the 8.2 kyr event (>7900 cal yr BP dated at 220 cm). This indicates that in the RdF (Fig. 11), the relative sea level reached at least the site VC7 during the 8.2 event, meanwhile the site CG2X was being eroded, as this core is located closer to a channel feature observed in seismic data (Fig. 2B), but the nearby site GC2P remained emerged (mainly cf. *Juncus*). Therefore, we can precise that during the 8.2 event the RSL in RdF remained stabilised at some level above −19.8 m NMMA but below −12.6 m NMMA.

Tree pollen succession observed in GC2P (Fig. 7) from the 8.2 kyr event until the Mid-Holocene (ca. 6600 cal yr BP) agrees with the regional pollen data available (Muñoz Sobrino et al., 2005; Iriarte-Chiapusso et al., 2016), but the pollen evidence in this site (with increasing abundances of Chenopodiaceae, dinoflagellate cysts and foraminiferal linings dated before 7860 cal yr BP) also indicates the local development of salt marsh vegetation. This evidence in cores VC7, CG2P and CG2X reveals a progressive RSL rise during that period (Fig. 11) and therefore allows a more precise palaeoenvironmental interpretation of the RSL changes in the RdF. In this connection, new data enable to distinguish the local development of marsh environments as part of a seismic unit (U6), which was previously mainly interpreted as tidal flat deposits (Cartelle et al., 2019).

Both the chronologies and the pollen data available for core VC3 (Fig. 8) disclose almost null marine influence at this point before 7470 yr BP (lack of Chenopodiaceae, with very scarce presence of dinoflagellates and foraminifera only appearing above 180 cm). Pollen abundance (concentration) along this section is variable but mostly low, including *Pinus*, Poaceae and Compositae, and three cf. *Juncus* maxima alternating with peaks of *Erica* and Cyperaceae (Fig. 8). This evidence suggests that before 7500 cal yr BP, this site remained emerged and was almost unaffected by tides (Fig. 11): i.e., forming part of ephemeral emerged ponds that might develop better (Fig. 9) during the three colder/moister stages just previously described in this sedimentary context (8.2, 9.3 and 10.5 cal kyr events).

All the sequences recovered in the inner part of RdF reveal a noticeable discontinuity (D6) in the sedimentary fill (Fig. 3). Reworking of coarse materials is very likely during highly dynamic phases of rapid sea-level rise (e.g. Fanget et al., 2016), particularly associated with the development of (tidal/wave) ravinement surfaces (Fig. 2). Therefore,

eventual inversions in the age-depth curves may be expected when dating levels of erosion related to seismic disconformities (Figs. 2 and 7). Considering this (Table 3), the conspicuous (D6) hiatus described in CG2P may be reasonably constrained between 6600 and 860 cal yr BP, so that the sequence restarts during the middle ages (11th century). At this moment, the high abundance of marine remains (dinoflagellate cysts and foraminiferal linings) agrees with the modern sea-level configuration (Fig. 11). Besides, the very low total tree pollen content indicates the regional deforestation, with the spread of heaths and the overrepresentation of alluvial forests (*Alnus*), high marshes (cf. *Juncus*), reed beds (mainly the Poaceae *Phragmites australis* (Cav.) Trin. ex Steud.) and chestnut crops (*Castanea*). Terrestrial contribution seems particularly high during the Little Ice Age, related to the Maunder Minimum (Fig. 11).

5.5. The new evidence within the environmental context of NW Iberia

Environmental dynamics described upon the new RdF data, including the main climatic events observed and their chronologies, largely agrees with the previous evidence described in other coastal ecosystems from NW Iberia, revealing the occurrence of noticeable changes in the regional RSL (e.g. Martínez-Carreño and García-Gil, 2017; Sáez et al., 2018; García-Moreiras et al., 2019a, 2019b; Gómez-Orellana et al., 2021). Particularly, during the transition between the Upper Pleistocene and the Early Holocene, several cold reversals (with oscillations of mean summer temperature between 1 and 2 °C) has been consistently described both at regional (e.g. Iriarte-Chiapusso et al., 2016; Muñoz Sobrino et al., 2013, 2018) and continental (e.g. Heiri et al., 2014) scales, which now may be directly connected with different episodes of stabilization (or minor drops) in the regional RSL. Besides, inferred summer mean temperatures corrected to modern sea level suggest that in the coastal areas of Atlantic NW Iberia, the July air temperatures rose from 15.5 to 21.5 °C between 15,600 and 10500 cal yr BP, whereas the modern mean July air temperature would amount to ca. 25 °C (Heiri et al., 2014). In this connection, it is presented here for the first time a consistent high-resolution space–time reconstruction of the impact of such changes on the coastal configuration and the coastal ecosystems inside a specific embayment, including the local evidence of rises of more than 10 m in RSL during the YD-Early Holocene transition (Fig. 11), which must be related to changes of only a few (<4°C) degrees in mean summer temperature in this region (Heiri et al., 2014). New local evidence of the regional stabilization of RSL is reported below than −12.6 m NMMA during the cold 8.2 event (Fig. 11).

This new evidence can have a substantive value for managing modern coastal areas threatened by the accelerated RSL, but also when interpreting the past environmental changes upland. In the coastal and inner mountains of NW Iberia, it has been consistently argued that the tree colonization of highlands and leeward slopes occurred during different stages of the Lateglacial to Holocene transition; and that this dynamic was probably driven by periods of general climatic warming that alternated with other short colder stages (e.g. Iriarte-Chiapusso et al., 2016; Muñoz Sobrino et al., 2018). The line of evidence showed here consistently demonstrate, for the first time in this region, that the regional relative sea-level oscillations combined with changes in the SST (e.g. García-Moreiras et al., 2019a, 2019b) could determinate the regional development, distribution, expansion or contraction of deciduous forests, coniferous woodlands, heathlands and also wetlands, as have been previously proposed upon other data exclusively acquired on oceanic or hyperoceanic highlands (e.g. Muñoz Sobrino et al., 2005, 2007, 2009, 2013). New pollen data (Figs. 5–8) also confirms that coniferous formations existed on the coastal lowlands during the Lateglacial and Early Holocene (*Pinus, Juniperus*), but then collapsed by the sea-level rise; and also that many demanding trees (*Quercus, Corylus, Carpinus, Taxus, Castanea, Arbutus*) remained sheltered on windward slopes during the coldest/driest stages until they began to colonize higher and inner sites as a consequence of the general climatic warming (e.g. Muñoz Sobrino et al., 2018; Gómez-Orellana et al., 2021).

6. Conclusions

We performed a multiproxy approach (that combined seismic, lithological, elemental, chronological and palynological data) to reconstruct the environmental changes that occurred during the Lateglacial-Holocene transition in a coastal embayment situated on a very climatic sensitive area from NW Iberia. The combination of elemental and pollen data allowed us to identify several levels representing local ecosystems dominated by *Juncus* sp., namely high-marshes, ephemeral emerged ponds or humid dune slacks. For the first time in this region, we were able to generate a consistent high-resolution spatial–temporal interpretation of the RSL changes using subtidal sediments from the same sub-basin (and thus free of substantial/differential post-depositional deformations) that describes in detail the flooding of the ancient coastal plains at the beginning of the Holocene. This includes new evidence of the sea level rising more than 10 m since the YD to the Early Holocene and different episodes of slowdown/stabilization occurring along this period, which can be related to the 11.4, 10.5 and 9.3 events. We provide local recording of a signal of sea-level stabilization below −12,6 m NMMA during the coldest stage of the Early Holocene, the 8.2 event. New evidence presented may also contribute to improve management of salt-marshes threatened by Global Change, and to enhance our understanding of the mechanisms driving the terrestrial ecosystem (coastal coniferous woodlands, deciduous forests, heathlands, wetlands) dynamics in NW Iberia during the Lateglacial and Holocene.

Declaration of Competing Interest

The authors declare that they have no known competing financial interests or personal relationships that could have appeared to influence the work reported in this paper.

Acknowledgements

References

Abrantes, F., 1991. Increased upwelling off Portugal during the last glaciation: Diatom evidence. Mar. Micropaleontol. 17 (3-4), 285–310.

Alonso, A., Pagés, J.L., 2010. Evolución del nivel del mar durante el Holoceno en el Noroeste de la Península Ibérica. Revista de la Sociedad Geológica de España 23, 157–167.

Alvarez, I., Gomez-Gesteira, M., deCastro, M., Lorenzo, M.N., Crespo, A.J.C., Dias, J.M., 2011. Comparative analysis of upwelling influence between the western and northern coast of the Iberian Peninsula. Cont. Shelf Res. 31 (5), 388–399. https://doi.org/10.1016/j.csr.2010.07.009.

Alves, J.M.R., Miranda, P.M.A., 2013. Variability of Iberian upwelling implied by ERA-40 and ERA-Interim reanalyses. Tellus 65 (1), 19245. https://doi.org/10.3402/tellusa:v65i0.19245.

Amami, B., Muller, S.D., Rhazi, L., Grillas, P., Rhazi, M., Bouahim, S., 2010. Modern pollen–vegetation relationships within a small Mediterranean temporary pool (western Morocco). Rev. Palaeobot. Palynol. 162 (2), 213–225. https://doi.org/10.1016/j.revpalbo.2010.06.012.

Arribas, J., Alonso, Á., Pagés, J.L., González-Acebrón, L., 2010. Holocene transgression recorded by sand composition in the mesotidal Galician coastline (NW Spain). Holocene 20 (3), 375–393.

Asensi, A., Diez-Garretas, B., 2017. Coastal Vegetation. In: Loidi, J. (Ed.): The Vegetation of the Iberian Penínusla, vol. 2, pp. 397–432. In: Werger, M.J.A. (series ed.): Plant and Vegetation, vol. 13. Springer, Utrecht, The Netherlands. http://dx.doi.10.1007/978-3-319-54867-8.

Baeteman, C., Waller, M., Kiden, P., 2011. Reconstructing middle to late Holocene sea-level change: a methodological review with particular reference to 'A new Holocene

sea-level curve for the southern North Sea' presented by K.-E. Behre. Boreas 40, 557–572. https://doi.org/10.1111/j.1502-3885.2011.00207.

Baltzer, A., Walter-Simonnet, A.-V., Mokeddem, Z., Tessier, B., Goubert, E., Cassen, S., Diffo, A., 2014. Climatically-driven impacts on sedimentation processes in the Bay of Quiberon (south Brittany, France) over the last 10,000 years. Holocene 24, 679–688.

Bao, R., da Conceição Freitas, M., Andrade, C., 1999. Separating eustatic from local environmental effects: a late-Holocene record of coastal change in Albufeira Lagoon, Portugal. Holocene 9, 341–352.

Barton, E.D., Largier, J.L., Torres, R., Sheridan, M., Trasviña, S., Souza, A., Pazos, Y., Valle-Levinson, A., 2015. Coastal upwelling and downwelling forcing of circulation in a semi-enclosed bay, Ria de Vigo. Prog. Oceanogr. 134, 173–189.

Behre, K.-E., 2007. A new Holocene sea-level curve for the southern North Sea. Boreas 36, 82–102.

Blaauw, M., 2010. Methods and code for 'classical' age-modelling of radiocarbon sequences. Quat. Geochronol. 5 (5), 512–518.

Bond, G., Showers, W., Cheseby, M., Lotti, R., Almasi, P., deMenocal, P., Priore, P., Cullen, H., Hajdas, I., Bonaniet, G., 1997. A pervasive millennial-scale cycle in the North Atlantic Holocene and glacial climates. Science 294, 2130–2136.

Boyd, R., Dalrymple, R.W., Zaitlin, B.A., 2006. Estuarine and incised-valley facies models. In: Posamentier, H.W., Walker, R.G. (Eds.), Facies Models Revisited, vol. 84. Society of Economic Paleontologists and Mineralogists Special Publication, pp. 171–235.

Boyle, J.F., 2000. Rapid elemental analysis of sediment samples by isotope source XRF. J. Paleolimnol. 23, 213–221.

Bungenstock, F., Schäfer, A., 2009. The Holocene relative sea-level curve for the tidal basin of the barrier island Langeoog, German Bight, Southern North Sea. Global Planet. Change 66, 34–51.

Bunting, M.J., 2003. Pollen–vegetation relationships in non-arboreal moorland taxa. Rev. Palaeobot. Palynol. 125, 285–298.

Cartelle, V., García-Gil, S., Plink-Björklund, P., 2019. From a river valley to a ria: Evolution of an incised valley (Ría de Ferrol, north-west Spain) since the Last Glacial Maximum. Sedimentology 66 (5), 1930–1966. https://doi.org/10.1111/sed.2019.66.issue-510.1111/sed.12565.

Cobelo-García, A., Prego, R., 2004. Influence of point sources on trace metal contamination and distribution in a semi-enclosed industrial embayment, the Ferrol Ria (NW Spain). Estuarine Coastal Shelf Science 60 (4), 695–703.

Crosby, S.C., Sax, D.F., Palmer, M.E., Booth, H.S., Deegan, L.A., Bertness, M.D., Leslie, H. M., 2020. Salt marsh persistence is threatened by predicted sea-level rise. Estuar. Coast. Shelf Sci. 181, 93–99. https://doi.org/10.1016/j.ecss.2016.08.018.

deCastro, M., Gomez-Gesteira, M., Prego, R., Neves, R., 2003. Wind influence on water exchange between the ria of Ferrol (NW Spain) and the shelf. Estuarine Coastal Shelf Science 56, 1055–1064.

deCastro, M., Gomez-Gesteira, M., Prego, R., Alvarez, I., 2004. Ria-ocean exchange driven by tides in the Ria of Ferrol (NW Spain). Estuarine Coastal Shelf Science 61, 15–24.

Dias, J.A.M., Boski, T., Rodrigues, A., Magalhaes, F., 2000. Coast line evolution in Portugal since the Last Glacial Maximum until present – A synthesis. Mar. Geol. 170, 177–186.

Di Rita, F., Celant, A., Milli, S., Magri, D., 2016. Lateglacial–early Holocene vegetation history of the Tiber delta (Rome, Italy) under the influence of climate change and sea level rise. Rev. Palaeobot. Palynol. 218, 204–216. https://doi.org/10.1016/j.revpalbo.2014.12.005.

Dorman, L.I., 2016. Chapter 20: Space Weather and Cosmic Ray Effects. In: Letcher, T.M. (Ed.), Climate Change, second ed. Elsevier, pp. 513–544. https://doi.org/10.1016/B978-0-444-63524-2.00030-0.

Dupont, L.M., Kuhlmann, H., 2017. Glacial-interglacial vegetation change in the Zambezi catchment. Quat. Sci. Rev. 155, 127–135. https://doi.org/10.1016/j.quascirev.2016.11.019.

Emmanouilidis, A., Unkel, I., Seguin, J., Keklikoglou, K., Gianni, E., Avramidis, P., 2020. Application of Non-Destructive Techniques on a Varve Sediment Record from Vouliagmeni Coastal Lake, Eastern Gulf of Corinth, Greece. Appl. Sci. 10, 8273. https://doi.org/10.3390/app10228273.

Erdtman, G., 1952. Pollen morphology and plant taxonomy: An Introduction to Palynology. Alqvist and Wiksell, Stockholm, Angiosperms.

Evans, D., 2006. The habitats of the European Union Habitats Directive. Biology and environment. Proceedings of the Royal Irish Academy 106B (3), 167–173.

Faegri, K., Iversen, J., 1964. Textbook of Pollen Analysis, 2nd Ed. Munksgaard, Copenhagen.

Fagherazzi, S., Mariotti, G., Leonardi, N., Canestrelli, A., Nardin, W., Kearney, W.S., 2020. Salt marsh dynamics in a period of accelerated sea level rise. e2019JF005200 J. Geophys. Res. Earth Surf. 125. https://doi.org/10.1029/2019JF005200.

Fanget, A.-S., Bassetti, M.-A., Fontanier, C., Tudryn, A., Berne, S., 2016. Sedimentary archives of climate and sea-level changes during the Holocene in the Rhonê prodelta (NW Mediterranean Sea). Clim. Past 12, 2161–2179. https://doi.org/10.5194/cp-12-2161-2016.

Ferdelman, T.G., Church, T.M., Luther, G.W., 1991. Sulfur enrichment of humic substances in a Delaware salt marsh sediment core. Geochim. Cosmochim. Acta 55, 979–988. https://doi.org/10.1016/0016-7037(91)90156-Y.

Fraga, F., 1981. Upwelling off the Galician Coast, Northwest Spain. In: Richardson, F.A. (Ed.), Coastal Upwelling. American Geophysical Union, Washington, pp. 176–182.

Fredskild, B., 1970. Palynological part. In: Degerbøl, M., Fredskild, B. (Eds.), The Urus (Bos primigenius bojanus) and Neolithic Domesticated Cattle (Bos taurus domesticus Linné) in Denmark. Kongelige Danske Videnskabernes Selskab Biologiske Skrifter, pp. 179–234.

García-Gil, S., De Blas, E., Martínez-Carreño, N., Iglesias, J., Rial-Otero, R., Simal-Gándara, J., Judd, A.G., 2011. Characterisation and preliminary quantification of the methane reservoir in a coastal sedimentary source: San Simón Bay, Ría de Vigo, NW Spain. Estuarine Coastal Shelf Science 91, 232–242.

García-Moreiras, I., Pospelova, V., García-Gil, S., Muñoz Sobrino, C., 2018. Climatic and anthropogenic impacts on the Ría de Vigo (NW Iberia) over the last two centuries: a high-resolution dinoflagellate cyst sedimentary record. Palaeogeogr. Palaeoclimatol. Palaeoecol. 504, 201–218. https://doi.org/10.1016/j.palaeo.2018.05.032.

García-Moreiras, I., Delgado, C., Martínez-Carreño, N., Garcia-Gil, S., Muñoz Sobrino, C., 2019a. Climate and vegetation changes in coastal ecosystems during the Middle Pleniglacial and the early Holocene: Two multi-proxy, high-resolution records from Ría de Vigo (NW Iberia). Global Planet. Change 176, 100–122. https://doi.org/10.1016/j.gloplacha.2019.02.015.

García-Moreiras, I., Cartelle, V., Garcia-Gil, S., Muñoz Sobrino, C., 2019b. First high-resolution multi-proxy palaeoenvironmental record of the Late Glacial to Early Holocene transition in the Ría de Arousa (Atlantic margin of NW Iberia). Quat. Sci. Rev. 215, 308–321. https://doi.org/10.1016/j.quascirev.2019.05.016.

García-Moreiras, I., Sánchez, J.M., Muñoz Sobrino, C., 2015. Modern pollen and non-pollen palynomorph assemblages of salt marsh and subtidal environments from the Ría de Vigo (NW Iberia). Rev. Palaeobot. Palynol. 219, 157–171. https://doi.org/10.1016/j.revpalbo.2015.04.006.

Gebregiorgis, D., Giosan, L., Hathorne, E.C., Anand, P., Nilsson-Kerr, K., Plass, A., Lückge, A., Clemens, S.C., Frank, M., 2020. What can we learn from X-ray fluorescence core scanning data? A paleomonsoon case study. e2019GC008414 Geochem. Geophys. Geosyst. 21. https://doi.org/10.1029/2019GC008414.

Gehrels, W.R., 1999. Middle and late Holocene sea-level changes in eastern Maine reconstructed from foraminiferal salt-marsh stratigraphy and AMS 14C dates of basal peat. Quat. Res. 52, 350–359.

Gerritse, R.G., George, R.J., 1988. The role of soil organic matter in the geochemical cycling of chloride and bromide. J. Hydrol. 101, 83–95.

Gómez-Gesteira, M., deCastro, M., Prego, R., Pérez-Villar, V., 2001. An unusual two layered tidal circulation induced by stratification and wind in the Ria of Pontevedra (NW Spain). Estuarine Coastal Shelf Science 52, 555–563.

Gómez-Orellana, L., Ramil-Rego, P., Ferreiro da Costa, J., Muñoz Sobrino, C., 2021. Holocene environmental change on the Atlantic coast of NW Iberia as inferred from the Ponzos wetland sequence. Boreas 50 (4), 1131–1145. https://doi.org/10.1111/bor.v50.410.1111/bor.12535.

Goy, JoséLuis, Zazo, C., Dabrio, C.J., Lario, J., Borja, F., Sierro, F.J., Flores, JoséAbel, 1996. Global and regional factors controlling changes of coastlines in Southern Iberia (Spain) during the Holocene. Quat. Sci. Rev. 15 (8-9), 773–780.

Grimm, E., 1990–2019. TILIA and TILIA.GRAPH: PC spreadsheets and graphics software for pollen data. INQUA Commission for the study of the Holocene Working Group Data Handling Methods. Newsletter 4, 5–7.

Hamilton, E.L., 1980. Geoacoustic modeling of the sea floor. J. Acoust. Soc. Am. 68, 1313–1340.

Hamilton, E.L., Bachman, R.T., 1982. Sound velocity and related properties of marine sediments. J Journal of the Acoustical Society of America 72, 1891–1904.

Heaton, T.J., Köhler, P., Butzin, M., Bard, E., Reimer, R.W., Austin, W.E.N., Bronk Ramsey, C., Grootes, P.M., Hughen, K.A., Kromer, B., Reimer, P.J., Adkins, J., Burke, A., Cook, M., Olsen, J., Skinner, L.C., 2020. Marine20 - the marine radiocarbon age calibration curve (0–55,000 cal BP). Radiocarbon 62 (4), 779–820. https://doi.org/10.1017/RDC.2020.68.

Heiri, H., Brooks, S.J., Renssen, H., Bedford, A., Hazekamp, M., Ilyashuk, B., Jeffers, E.S., Lang, B., Kirilova, E., Kuiper, S., Millet, L., Samartin, S., Toth, M., Verbruggen, F., Watson, J.E., van Asch, N., Lammertsma, E., Amon, L., Birks, H.H., Birks, H.J.B., Mortensen, M.F., Hoek, W.Z., Magyari, E., Muñoz Sobrino, C., Seppa, H., Tinner, W., Tonkov, S., Veski, S., Lotter, A.F., 2014. Validation of climate model-inferred regional temperature change for late-glacial Europe. Nat. Commun. 5, 4914. https://doi.org/10.1038/ncomms5914.

Houston, J.A., 2008. Management of Natura 2000 habitats. 2190 Humid dune slacks. European Commission. Technical Report 2008 05/24.

IGME (Instituto Geologico y Minero de España), 1981. Mapa geológico de España e 1,50000. Ministerio de Industria y Energía Publishing Service, Madrid.

Iriarte-Chiapusso, M.J., Muñoz Sobrino, C., Gómez-Orellana, L., Hernández-Beloqui, B., García-Moreiras, I., Fernández Rodriguez, C., Heiri, O., Lotter, A.F., Ramil-Rego, P., 2016. Reviewing the Lateglacial-Holocene transition in NW Iberia: a palaeoecological approach based on the comparison between dissimilar regions. Quat. Int. 403, 211–236.

Justino, F., Peltier, W.R., 2005. The glacial North Atlantic Oscillation. Geophys. Res. Lett. 32, L21803. https://doi.org/10.1029/2005GL023822.

Kearney, M.S., 2001. Late Holocene sea level variation. In: Douglas, B.C., Kearney, M.S., Leatherman, S. (Eds.), Sea Level Rise, History and Consequences, 13–36. Academic Press, San Diego.

Leorri, Eduardo, Fatela, Francisco, Drago, Teresa, Bradley, Sarah Louise, Moreno, João, Cearreta, Alejandro, 2013. Lateglacial and Holocene coastal evolution in the Minho estuary (N Portugal): Implications for understanding sea-level changes in Atlantic Iberia. The Holocene 23 (3), 353–363. https://doi.org/10.1177/0959683612460786.

Lorenzo, M.N., Taboada, J.J., Gimeno, L., 2008. Links between circulation weather types and teleconnection patterns and their influence on precipitation patterns in Galicia (NW Spain). Int. J. Climatol. 28, 1493–1505. https://doi.org/10.1002/joc.1646.

Lu, Q., Bai, J., Gao, G., Wang, J., Zhao, Q., 2016. Effects of Water Level and Salinity on Total Sulfur Contents in Salt Marsh Soils of the Yellow River Delta, China. Wetlands 36 (Suppl 1), S137–S143. https://doi.org/10.1007/s13157-015-0661-3.

Matero, I.S.O., Gregoire, L.J., Ivanovic, R.F., Tindall, J.C., Haywood, A.M., 2017. The 8.2 ka cooling event caused by Laurentide ice saddle collapse. Earth Planet. Sci. Lett. 473, 205–214.

Marsh, P.E., Cohen, A.D., 2008. Identifying high-level salt marshes using a palynomorphic fingerprint with potential implications for tracking sea level change. Rev. Palaeobot. Palynol. 148, 60–69.

Martínez-Carreño, N., García-Gil, S., 2017. Reinterpretation of the Quaternary sedimentary infill of the Ría de Vigo, NW Iberian Peninsula, as a compound incised valley. Quat. Sci. Rev. 173, 124–144.

McCarthy, F.M.G., Mudie, P.J., 1998. Oceanic pollen transport and pollen: dinocyst ratios as markers of late Cenozoic sea level change and sediment transport. Palaeogeogr. Palaeoclimatol. Palaeoecol. 138, 187–206.

Mitchum Jr., R.M., Vail, P.R., Sangree, J.B., 1977. Seismic stratigraphy and global changes of sea level, part 6, stratigraphic interpretation of seismic reflection patterns in depositional sequences. In: Payton, C.E. (Ed.), Seismic Stratigraphy – Applications to Hydrocarbon Exploration, vol. 26. American Association of Petroleum Geologists Memoir, pp. 135–144.

Moore, P.D., Webb, J.A., Collinson, M.E., 1991. Pollen Analysis. Blackwell, London, p. 216.

Moreno, A., Svensson, A., Brooks, S.J., Connor, S., Engels, S., Fletcher, W., Genty, D., Heiri, O., Labuhn, I., Persoiui, A., Peyron, O., Sadori, L., Valero-Garces, B., Wulf, S., Zanchetta, G., data contributors, 2014. A compilation of Western European terrestrial records 60–8 ka BP: towards an understanding of latitudinal climatic gradients. Quat. Sci. Rev. 106, 167–185.

Moreno, J., Fatela, F., Leorri, E., Araújo, M.F., Moreno, F., De la Rosa, J., Freitas, M.C., Valente, T., Corbett, D.R., 2015. Bromine enrichment in marsh sediments as a marker of environmental changes driven by Grand Solar Minima and anthropogenic activity (Caminha, NW of Portugal). Sci. Total Environ. 506–507, 554–566.

Muñoz Sobrino, C., Ramil Rego, P., Rodríguez Guitián, M., 2001. Vegetation in the mountains of NW Iberia during the last glacial-interglacial transition. Veget. Hist. Archaeobot. 10, 7–21.

Muñoz Sobrino, C., Ramil-Rego, P., Gómez-Orellana, L., Díaz Varela, R.A., 2005. Palynological data on major Holocene climatic events in NW Iberia. Boreas 34, 381–400.

Muñoz Sobrino, C., García-Gil, S., Diez, J.B., Iglesias, J., 2007. Palynological characterization of gassy sediments in the inner part of Ría de Vigo (NW Spain). New chronological and environmental data. Geo-Mar. Lett. 27 (2–4), 289–302.

Muñoz Sobrino, C., Ramil-Rego, P., Gómez-Orellana, L., Ferreiro da Costa, J., Díaz Varela, R.A., 2009. Climatic and human effects on the post-glacial dynamics of Fagus sylvatica L in NW Iberia. Plant Ecol. 203, 317–340.

Muñoz Sobrino, C., García-Gil, S., Iglesias, J., Martínez-Carreño, N., Ferreiro da Costa, J., Díaz Varela, R.A., Judd, A., 2012. Environmental change in the Ría de Vigo, NW Iberia, since the mid-Holocene: new palaeoecological and seismic evidence. Boreas 41, 578–601.

Muñoz Sobrino, C., García-Moreiras, I., Castro, Y., Martínez Carreño, N., de Blas, E., Fernández Rodríguez, C., Judd, A., García-Gil, S., 2014. Climate and anthropogenic factors influencing an estuarine ecosystem from NW Iberia: new high resolution multiproxy analyses from San Simón Bay (Ría de Vigo). Quat. Sci. Rev. 93, 11–33. https://doi.org/10.1016/j.quascirev.2014.03.021https://doi.org/10.1016/jquascirev201403021.

Muñoz Sobrino, C., García-Moreiras, I., Martínez-Carreño, N., Cartelle, V., Insua, T.L., Ferreiro Da Costa, J., Ramil-Rego, P., Fernández Rodríguez, C., Alejo, I., García-Gil, S., 2016. Reconstruction of the environmental history of a coastal insular system using shallow marine records: the last three millennia of the Cíes Islands (Ría de Vigo, NW Iberia). Boreas 45, 729–753. https://doi.org/10.1111/bor.12178.

Muñoz Sobrino, C., Heiri, O., Hazekamp, M., van der Velden, D., Kirilova, E.P., García-Moreiras, I., Lotter, A.F., 2013. New data on the Lateglacial period of SW Europe: a high-resolution multiproxy record from Laguna de la Roya (NW Iberia). Quat. Sci. Rev. 80, 58–77.

Muñoz Sobrino, Castor, García-Moreiras, Iria, Gómez-Orellana, Luis, Iriarte-Chiapusso, María José, Heiri, Oliver, Lotter, André F., Ramil-Rego, Pablo, 2018. The last hornbeam forests in SW Europe: new evidence on the demise of *Carpinus betulus* in NW Iberia. Vegetation History and Archeobotany 27 (4), 551–576. https://doi.org/10.1007/s00334-017-0654-7.

Otero, P., Ruiz-Villarreal, M., Peliz, A., 2008. Variability of river plumes off Northwest Iberia in response to wind events. J. Mar. Syst. 72, 238–255.

Paterson, D.M., Hanley, N.D., Black, K., Defew, E.C., Solan, M. (Eds.), 2011. Biodiversity, Ecosystems and Coastal Zone Management: Linking Science and Policy. Mar. Ecol. Progr. Ser., 434, 201–301. https://doi.org/10.3354/meps09279.

Peltier, W.R., 2001. Global glacial isostatic adjustment and modern instrumental records of relative sea-level history. In: Douglas, B.C., Kearney, M.S., Leatherman, L. (Eds.), Sea-Level Rise, History and Consequences, 65–95. Academic Press, San Diego.

Perillo, G.M.E., Wolanski, E., Cahoon, D.R., Brinson, M.M. (Eds.), 2009. Coastal Wetlands: An Integrated Ecosystem Approach. Elsevier, Amsterdam.

Poirier, C., Tessier, B., Chaumillon, E., 2017. Climate control on late Holocene high-energy sedimentation along coasts of the northeastern Atlantic Ocean. Palaeogeogr. Palaeoclimatol. Palaeoecol. 485, 784–797.

Pratolongo, P.D., Kirby, J.R., Plater, A., Brinson, M.M., 2009. Temperate coastal wetlands: morphology, sediment processes and plant communities. In: Perillo, G.M. E., Wolanski, E., Cahoon, D.R., Brinson, M.M. (Eds.), Coastal Wetlands: An Integrated Ecosystem Approach, 119–156. Elsevier, Amsterdam.

Prego, R., Dale, A.W., deCastro, M., Gomez-Gesteira, M., Taboada, J.J., Montero, P., Ruiz-Villarreal, M., Pérez-Villar, V., 2001. Hydrography of the Pontevedra Ria, intraannual spatial and temporal variability in a Galician coastal system (NW Spain). J. Geophys. Res. 106, 19845–19857.

Prego, R., Varela, M., 1998. Hydrography of the Artabro Gulf in summer, western coastal limit of Cantabrian seawater and wind-induced upwelling at Prior Cape. Oceanol. Acta 2, 145–156.

Rasmussen, S.O., Bigler, M., Blockley, S.P., Blunier, T., Buchardt, S.L., Clausen, H.B., Cvijanovic, I., Dahl-Jensen, D., Johnsen, S.J., Fischer, H., Gkinis, V., Guillevic, M., Hoek, W.Z., Lowe, J.J., Pedro, J.B., Popp, T., Seierstad, I.K., Steffensen, J.P., Svensson, A.M., Vallelonga, P., Vinther, B.M., Walker, M.J., Wheatley, J.J., Winstrup, M., 2014. A stratigraphic framework for abrupt climatic changesduring the Last Glacial period based on three synchronized Greenland ice-corerecords: refining and extending the INTIMATE event stratigraphy. Quat. Sci. Rev. 106, 14e28. https://doi.org/10.1016/j.quascirev.2014.09.007.

Rea, B.R., Pellitero, R., Spagnolo, M., Hughes, P., Ivy-Ochs, S., Renssen, H., Ribolini, A., Bakke, J., Lukas, S., Braithwaite, R.J., 2020. Atmospheric circulation over Europe during the Younger Dryas. Science. Advances 6, eaba4844.

Reimer, Paula J, Austin, William E N, Bard, Edouard, Bayliss, Alex, Blackwell, Paul G, Bronk Ramsey, Christopher, Butzin, Martin, Cheng, Hai, Edwards, R Lawrence, Friedrich, Michael, Grootes, Pieter M, Guilderson, Thomas P, Hajdas, Irka, Heaton, Timothy J, Hogg, Alan G, Hughen, Konrad A, Kromer, Bernd, Manning, Sturt W, Muscheler, Raimund, Palmer, Jonathan G, Pearson, Charlotte, van der Plicht, Johannes, Reimer, Ron W, Richards, David A, Scott, E Marian, Southon, John R, Turney, Christian S M, Wacker, Lukas, Adolphi, Florian, Büntgen, Ulf, Capano, Manuela, Fahrni, Simon M, Fogtmann-Schulz, Alexandra, Friedrich, Ronny, Köhler, Peter, Kudsk, Sabrina, Miyake, Fusa, Olsen, Jesper, Reinig, Frederick, Sakamoto, Minoru, Sookdeo, Adam, Talamo, Sahra, 2020. The IntCal20 Northern Hemisphere radiocarbon age calibration curve (0–55 cal kBP). Radiocarbon 62 (4), 725–757. https://doi.org/10.1017/RDC.2020.41.

Rodríguez, J.F., Saco, P.M., Sandi, S., Saintilan, N., Riccardi, G., 2017. Potential increase in coastal wetland vulnerability to sea-level rise suggested by considering hydrodynamic attenuation effects. Nat. Commun. 8, 16094. https://doi.org/10.1038/ncomms16094.

Rothwell, R.G., Croudace, I.W., 2015. Chapter 2: twenty years of XRF core scanning marine sediments: what do geochemical proxies tell us? In: Croudace, I.W., Rothwell, R.G. (Eds.): Micro-XRF Studies of Sediment Cores. Developments in Paleoenvironmental Research, vol. 17, pp. 25–102.

Roucoux, K.R., Shackleton, N.J., de Abreu, L., Schönfeld, J., Tzedakis, P.C., 2001. Combined marine proxy and pollen analyses reveal rapid Iberian vegetation response to North Atlantic millennial-scale climate oscillations. Quat. Res. 56, 128–132.

Sáez, Alberto, Carballeira, Rafael, Pueyo, Juan J., Vázquez-Loureiro, David, Leira, Manel, Hernández, Armand, Valero-Garcés, Blas L., Bao, Roberto, Girardclos, Stéphanie, 2018. Formation and evolution of back-barrier perched lakes in rocky coasts: An example of a Holocene system in north-west Spain. Sedimentology 65 (6), 1891–1917. https://doi.org/10.1111/sed.2018.65.issue-610.1111/sed.12451.

Shennan, I., Horton, B., 2002. Holocene land- and sea-level changes in Great Britain. J. Quat. Sci. 17 (5–6), 511–526.

Silva, J.P., Phillips, L., Jones, W., Eldridge, J., O'Hara, E., 2007. LIFE and Europe's wetlands. Restoring a Vital Ecosystem. Office for Official Publications of the European Communities, Brussels, p. 68.

Smith, D.E., Harrison, S., Firth, C.R., Jordan, J.T., 2011. The early Holocene sea-level rise. Quat. Sci. Rev. 30, 1846–1860.

Soares, António Monge, Dias, João M Alveirinho, 2007. Reservoir effect of coastal waters off western and northwestern Galicia. Radiocarbon 49 (2), 925–936.

Sorrel, P., Debret, M., Billeaud, I., Jaccard, S.L., McManus, J.F., Tessier, B., 2012. Persistent non-solar forcing of Holocene storm dynamics in coastal sedimentary archives. Nature Geosciences 5, 892.

Sprangers, M., Dammers, N., Brinkhuis, H., van Weering, T.C.E., Lotter, A.F., 2004. Modern organic-walled dinoflagellate cyst distribution offshore NW Iberia; tracing the upwelling system. Rev. Palaeobot. Palynol. 128, 97–106.

Stancliffe, R.P.W., 2002. Microforaminiferal linings. In: Jansonius, J., McGregor, D.C. (Eds.), Palynology: Principles and Applications 1, 373–379. American Association of Stratigraphical Palynologists Foundation, Dallas.

Stuiver, M., Reimer, P.J., Reimer, R.W., 2020. CALIB 8.2 [WWW program] at http://calib.org, accessed 2020-11-5.

Troiani, B.T., Simms, A.R., Dellapenna, T., Piper, E., Yokoyama, Y., 2011. The importance of sea-level and climate change, including changing wind energy, on the evolution of a coastal estuary: Copano Bay, Texas. Mar. Geol. 280, 1–19.

Turner, Jonathan N., Holmes, Naomi, Davis, Stephen R., Leng, Melanie J., Langdon, Catherine, Scaife, Robert G., 2015. A multiproxy (micro-XRF, pollen, chironomid and stable isotope) lake sediment record for the Lateglacial to Holocene transition from Thomastown Bog, Ireland. J. Quat. Sci. 30 (6), 514–528.

van Asperen, E.N., Kirby, J.R., Hunt, C.O., 2016. The effect of preparation methods on dung fungal spores: Implications for recognition of megafaunal populations. Rev. Palaeobot. Palynol. 229, 1–8.

van der Knaap, W.O., van Leeuwen, J.F.N., 1997. Late Glacial and Early Holocene vegetation succession altitudinal vegetation zonation, and climatic change in the Serra da Estrela, Portugal. Rev. Palaeobot. Palynol. 97, 239–285.

van Geel, B., 2003. Non pollen palynomorphs. In: Smol, J.P., Birks, H.J.B., Last, W.M. (Eds.), Tracking Environmental Change Using Lake Sediments 3, Terrestrial, Algal and Siliceous Indicators, 99–120. Kluwer Academic, Dordrecht.

van Geel, B., Coope, G.R., van der Hammen, T., 1989. Palaeoecology and stratigraphy of the Lateglacial type section at Usselo (The Netherlands). Rev. Palaeobot. Palynol. 60, 25–129.

Vink, Annemiek, Steffen, Holger, Reinhardt, Lutz, Kaufmann, Georg, 2007. Holocene relative sea-level change, isostatic subsidence and the radial viscosity structure of the mantle of northwest Europe (Belgium, the Netherlands, Germany, southern North Sea). Quat. Sci. Rev. 26 (25-28), 3249–3275.

Waller, M., Carvalho, F., Grant, M.J., Bunting, M.J., Brown, K., 2017. Disentangling the pollen signal from fen systems: Modern and Holocene studies from southern and eastern England. Rev. Palaeobot. Palynol. 238, 15–33.

Wanner, H., Mercolli, L., Grosjean, M., Ritz, S.P., 2015. Holocene climate variability and change; a data-based review. J. Geol. Soc. 172, 254–263. https://doi.org/10.1144/jgs2013e101.

Wasmind, K., Mussmann, M., Loy, A., 2017. The life sulfuric: microbial ecology of sulfur cyclingin marine sediments. Environ. Microbiol. Rep. 9 (4), 323–344.

Wentworth, Chester K., 1922. A scale of grade and class terms for clastic sediments. J. Geol. 30 (5), 377–392.

Wiessner, A., Kuschk, P., Nguyen, P.M., Müllera, J.A., 2017. The sulfur depot in the rhizosphere of a common wetland plant, Juncus effusus, can support long-term dynamics of inorganic sulphur transformations. Chemosphere 184, 375–383. https://doi.org/10.1016/j.chemosphere.2017.06.016.

Wiessner, A., Rahman, K.Z., Kuschk, P., Kästner, M., Jechorek, M., 2010. T Dynamics of sulphur compounds in horizontal sub-surfaceflow laboratory-scale constructed wetlands treating artificial sewage. Water Res. 44 (20), 6175–6185. https://doi.org/10.1016/j.watres.2010.07.044.

Zhao, Xueqin, Dupont, Lydie, Cheddadi, Rachid, Kölling, Martin, Reddad, Hanane, Groeneveld, Jeroen, Ain-Lhout, Fatima Zohra, Bouimetarhan, Ilham, 2019. Recent climatic and anthropogenic impacts on endemic species in southwestern Morocco. Quat. Sci. Rev. 221, 105889. https://doi.org/10.1016/j.quascirev.2019.105889.

Zonneveld, Karin A.F., Marret, Fabienne, Versteegh, Gerard J.M., Bogus, Kara, Bonnet, Sophie, Bouimetarhan, Ilham, Crouch, Erica, de Vernal, Anne, Elshanawany, Rehab, Edwards, Lucy, Esper, Oliver, Forke, Sven, Grøsfjeld, Kari, Henry, Maryse, Holzwarth, Ulrike, Kielt, Jean-François, Kim, So-Young, Ladouceur, Stéphanie, Ledu, David, Chen, Liang, Limoges, Audrey, Londeix, Laurent, Lu, S.-H., Mahmoud, Magdy S., Marino, Gianluca, Matsouka, Kazumi, Matthiessen, Jens, Mildenhal, D.C., Mudie, Peta, Neil, H.L., Pospelova, Vera, Qi, Yuzao, Radi, Taoufik, Richerol, Thomas, Rochon, André, Sangiorgi, Francesca, Solignac, Sandrine, Turon, Jean-Louis, Verleye, Thomas, Wang, Yan, Wang, Zhaohui, Young, Marty, 2013. Atlas of modern dinoflagellate cyst distribution based on 2405 datapoints. Rev. Palaeobot. Palyn. 191, 1–197.